

RECEIVED

MAR 25 1996

OSTI

*Atmospheric Transport of  
Neutrons and Gamma Rays from  
Near-Horizon Nuclear Detonations*

DISCLAIMER

This report was prepared as an account of work sponsored by an agency of the United States Government. Neither the United States Government nor any agency thereof, nor any of their employees, makes any warranty, express or implied, or assumes any legal liability or responsibility for the accuracy, completeness, or usefulness of any information, apparatus, product, or process disclosed, or represents that its use would not infringe privately owned rights. Reference herein to any specific commercial product, process, or service by trade name, trademark, manufacturer, or otherwise does not necessarily constitute or imply its endorsement, recommendation, or favoring by the United States Government or any agency thereof. The views and opinions of authors expressed herein do not necessarily state or reflect those of the United States Government or any agency thereof.

**Los Alamos**  
NATIONAL LABORATORY

*Los Alamos National Laboratory is operated by the University of California  
for the United States Department of Energy under contract W-7405-ENG-36.*

DISTRIBUTION OF THIS DOCUMENT IS UNLIMITED

**MASTER**

*Edited by Martha Lee DeLanoy, Group CIC-1*

*This work was supported by the U.S. Department of Energy, Office of Research and Development of the Office of Nonproliferation and National Security.*

*An Affirmative Action/Equal Opportunity Employer*

*This report was prepared as an account of work sponsored by an agency of the United States Government. Neither The Regents of the University of California, the United States Government nor any agency thereof, nor any of their employees, makes any warranty, express or implied, or assumes any legal liability or responsibility for the accuracy, completeness, or usefulness of any information, apparatus, product, or process disclosed, or represents that its use would not infringe privately owned rights. Reference herein to any specific commercial product, process, or service by trade name, trademark, manufacturer, or otherwise, does not necessarily constitute or imply its endorsement, recommendation, or favoring by The Regents of the University of California, the United States Government, or any agency thereof. The views and opinions of authors expressed herein do not necessarily state or reflect those of The Regents of the University of California, the United States Government, or any agency thereof. The Los Alamos National Laboratory strongly supports academic freedom and a researcher's right to publish; therefore, the Laboratory as an institution does not endorse the viewpoint of a publication or guarantee its technical correctness.*

*Atmospheric Transport of  
Neutrons and Gamma Rays from  
Near-Horizon Nuclear Detonations*

R. C. Byrd  
B. D. Heerema\*

\*HQ AFTAC/DOSD, Patrick Air Force Base, FL 32925.

**Los Alamos**  
NATIONAL LABORATORY  
Los Alamos, New Mexico 87545

DISTRIBUTION OF THIS DOCUMENT IS UNLIMITED



# ATMOSPHERIC TRANSPORT OF NEUTRONS AND GAMMA RAYS FROM NEAR-HORIZON NUCLEAR DETONATIONS

by

R. C. Byrd and B. D. Heerema

## ABSTRACT

This report continues a study of the transport of neutrons and gamma rays from nuclear detonations at high altitudes to a set of orbiting detectors, with an emphasis on the limiting case of sources near and even beyond the horizon. To improve the calculational efficiency, the standard arrangement of a single source with multiple detectors is transformed to an equivalent one with a single detector and sources at multiple locations. Particular attention is paid to the critical problem of transport at near-horizon angles in an atmosphere whose density decreases exponentially with altitude. As a check, calculations for this region are made using both analytical and Monte Carlo approaches. For sources approaching the horizon, the fluence of gamma rays and neutrons reaching the detector drops gradually as the increasing column density attenuates the direct, unscattered fluence. Near the grazing angle, the direct fluence plummets, but the scattered component continues to decrease slowly and remains observable. Over this range, the time-dependent flux of direct-plus-scattered gamma rays changes dramatically in both shape and magnitude, but it probably remains distinct from typical natural backgrounds. The neutron time-of-flight spectrum is dominated by scattering and reflects only the most important aspects of the original source spectrum; its most obvious features are a prominent low-energy tail and the resonance structure produced by nuclear interactions in the atmosphere. In some cases, the fluence of secondary gamma rays produced by these interactions may be larger than that from the source itself.

---

## 1. INTRODUCTION

**Motivation.** Although the behavior of nuclear detonations in free space is easily understood, for atmospheric explosions the signals reaching space-based detectors can be greatly distorted. Many of the features of this distortion can be studied using calculations with generic sources, such as instantaneous bursts of gamma rays with an evaporation spectrum or neutrons with Maxwell fission and Gaussian fusion spectra. The important observables are the intensities and the time or energy dependences of the fluences

reaching the detector. Some of these signatures can be estimated by simple attenuation calculations, but obtaining a complete picture requires using Monte Carlo simulations to handle the large amount of atmospheric scattering. Furthermore, as the path between the source and detector approaches the horizon, the exponentially increasing density of the atmosphere and the rapidly lengthening path integral require that these cases be handled carefully to ensure accurate results. This report is aimed specifically at these problems.

**Previous Work.** An earlier report<sup>1</sup> described the basic calculations for gamma-ray and neutron transport from a nuclear detonation high in the atmosphere to detectors located on orbiting satellites; most readers should consult a copy as background for the present work. The source altitudes varied from 20 km to 50 km, which is above 95–99% of the total depth of the nearly exponential atmosphere.<sup>2</sup> The detectors were placed in 100-km and geosynchronous orbits at elevation angles from 90° (vertically overhead) to –5° (just below the horizon). All calculations were made using the MCNP (Monte Carlo N-Particle) transport code<sup>3</sup> developed at Los Alamos National Laboratory (LANL). The unscattered fluence followed the expected attenuation behavior and dropped rapidly as the horizon was approached, but the scattered fluence remained detectable out to the most extreme angles. Because the previous study was not optimized for near-horizon geometries, however, its results in this region had poor statistical accuracies. The present study addresses this problem by introducing some of the more powerful techniques available with the MCNP code.

**Contents.** Chapter 2 lays out the framework for the MCNP calculations, emphasizing the changes from the previous study. Chapter 3 addresses gamma-ray transport, discussing the angle dependence of the integrated fluences, the shapes of the energy spectra in the horizon region, and especially the effect of scattering on the time-of-arrival spectra at high latitudes. Chapter 4 covers much the same material for the neutron case, but it includes the important separation between fission and fusion sources and the relationship between neutron energy spectra and time-of-flight measurements. Chapter 5 briefly compares the gamma-ray fluence produced by  $(n,n'\gamma)$  reactions in the atmosphere with that from the original source. Chapter 6 summarizes the results and suggests areas for additional study.

## 2. CALCULATION LAYOUT

**Overview.** This chapter discusses three improvements in the previous analysis that are particularly important for the case of near-horizon transport. First, a coordinate transformation is used to modify the standard Monte Carlo arrangement, where a single source generates particles that are tallied at multiple detector locations. Second, finer graduations are introduced in the segmented approximation for the atmosphere's near-exponential density dependence, which allows better fidelity for near-horizon angles and for scattering trajectories that carry particles upward and over the horizon. Third, an analytical solution to the gamma-ray transport problem is formulated using integrated column densities and tabulated attenuation coefficients, and the results are compared with the Monte Carlo calculations.

## 2.1. GEOMETRY TRANSFORMATION

**Original Calculation Geometry.** In Fig. 2.1, which is adapted from Ref. 1, we show the standard source-and-detector geometry for the current problem. We have arranged the figure to emphasize a polar view of the source ( $S$ ) and ten detector locations ( $D_1, D_2, \dots, D_{10}$ ), which are all confined to the equatorial plane of a *geostationary* orbit. Because the transport calculations make no reference to the Earth's rotation, however, the orbital plane could be any geosynchronous orbit, and the pole in Fig. 2.1 would refer not to the axis of the Earth's rotation, but to the axis of the detector orbit. Although the geometry shown in Fig. 2.1 is convenient for the MCNP calculations, it is not the most general or realistic case, especially for the present study of near-horizon transport.

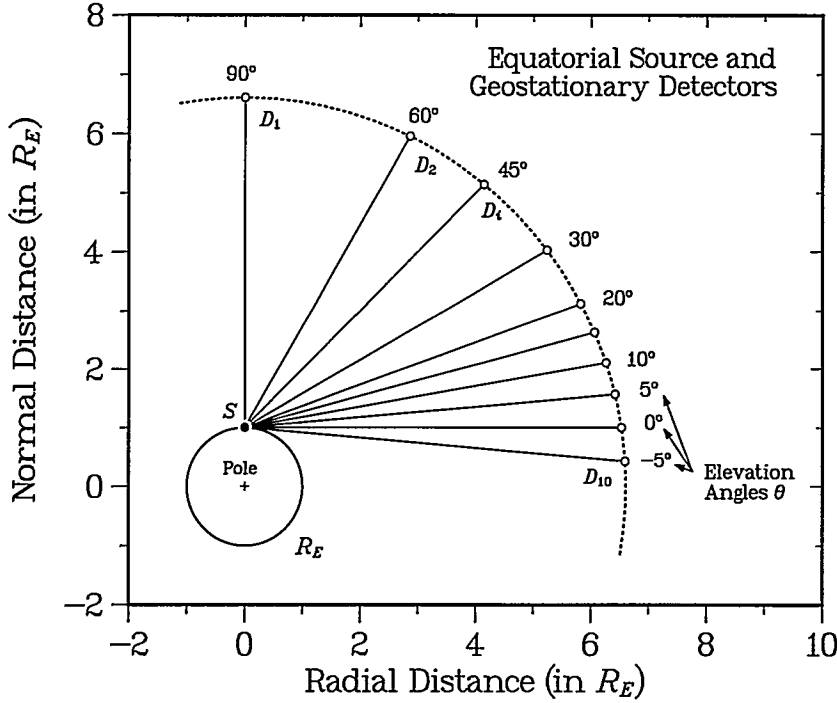
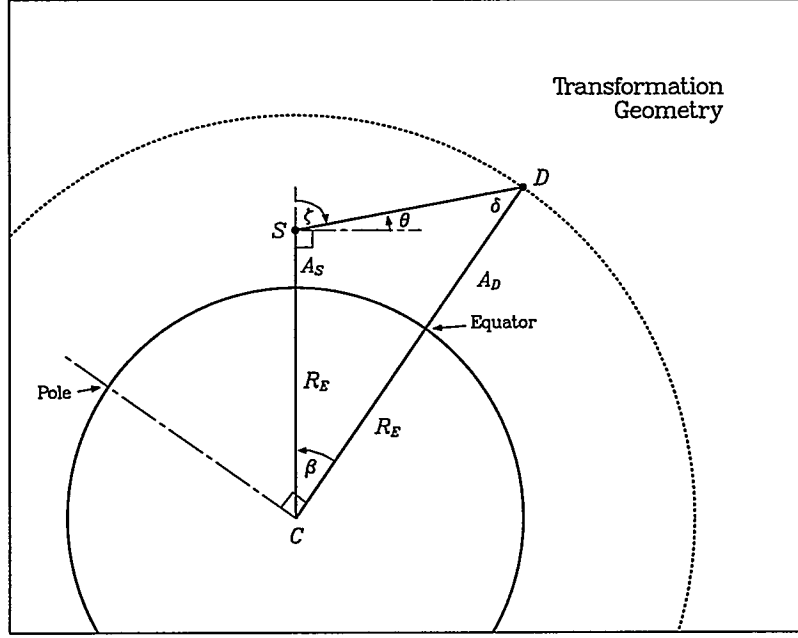


Fig. 2.1. Scale illustration of the geometry for the calculations, looking downward from above the pole onto an equatorial source with detector locations in a geostationary orbit at elevation angles between  $90^\circ$  (above the source) and  $-5^\circ$  (below the local horizon).

**Alternative Source-and-Detector Geometries.** The arrangement in Fig. 2.1 allows a single MCNP calculation to accumulate multiple detector tallies simultaneously for a source at a particular location. However, an equally interesting problem is that of a single geosynchronous detector with sources at different angles, which would normally require multiple MCNP runs. Instead, we can use the relationships shown in Fig. 2.2 to transform this single-source case into a single-detector geometry. Here the source  $S$  is located at a central angle  $\beta$  and altitude  $A_S$  above a spherical Earth of radius  $R_E$ . The detector  $D$  is in a geosynchronous orbit at an altitude  $A_D$  above the surface. The angle  $\theta$  is the elevation angle above the source's local horizon, which is related to the local zenith angle as  $\zeta = \pi/2 - \theta$ . For each source altitude  $A_S$ , multiple tallies for all detectors  $D_i$



**Fig. 2.2.** Geometrical relationships (not to scale) for converting a single source with multiple detectors to a single detector with multiple sources. The source altitude  $A_S$ , detector altitude  $A_D$ , and elevation angle  $\theta$  are quantities that define the central angle  $\beta$ .

at elevation angles  $\theta_i$  can be accumulated in a single MCNP run. To transform to the equivalent case of a single detector  $D$  with multiple sources  $S_i$ , we need an expression for  $\beta$  in terms of  $\theta$ . From triangle  $CSD$ ,

$$R_S \sin(\pi/2 + \theta) = R_D \sin \delta ,$$

where  $R_S = R_E + A_S$ ,  $R_D = R_E + A_D$ , and the angles  $\delta$  and  $\beta$  are related by

$$\beta = \frac{\pi}{2} - \theta - \delta .$$

Combining these two equations and solving for  $\beta$  gives

$$\beta = \frac{\pi}{2} - \theta - \arctan \left( \frac{R_S \sin(\pi/2 + \theta)}{\sqrt{R_D^2 - R_S^2 \sin^2(\pi/2 + \theta)}} \right) , \quad (2.1)$$

where the arctangent function is used for compatibility with standard FORTRAN. Table 2.1 lists the elevation angles  $\theta_i$  used in Ref. 1 along with the corresponding central angles  $\beta_i$ .

**Transformed Geometry.** In Fig. 2.3a we show the transformed single-detector version of the single-source geometry in Fig. 2.1. Again, the tallies for the multiple sources  $S_1, S_2, \dots, S_{10}$  are actually accumulated in a single MCNP calculation using the original geometry. The transformation is then used to rearrange the source-to-detector paths so they converge at the detector instead of the source, keeping the relationship between the



**Table 2.1.** Transformation of Elevation Angle  $\theta$  to Central Angle  $\beta$ .

Index	Elevation Angle $\theta$	Central Angle $\beta$
1	-5	86.3
2	0	81.3
3	5	76.3
4	10	71.4
5	15	66.6
6	20	61.8
7	30	52.4
8	45	38.8
9	60	25.6
10	90	0.0

Earth, source, and detector exactly the same for each path. The impact of this rearrangement is emphasized in Fig. 2.3b, which shows a closer view of the connection between the single geosynchronous detector  $D$  and the multiple sources at elevation angles  $\theta$  or central angles  $\beta$ . Here the open circles are the transformed versions of the 10 angles in Table 2.1 for the previous calculations, and the solid circles are the 20 angles for the present work in the horizon region. Just as the previous angles were chosen in integer increments of  $\theta$ , the present calculations use integer values of  $\beta$  between  $60^\circ$  and  $100^\circ$ , which are listed in Table 2.2. For situations in which elevation angles  $\theta$ , not central angles  $\beta$ , are desired, this table also provides the necessary conversion. Again, we emphasize that results for all 20 angles (the maximum allowed by MCNP) were tallied using six main MCNP runs, three each for gamma rays and neutrons, with sources at 20, 30, and 50 km. Supplemental runs were used to provide high-resolution time-of-arrival spectra for the gamma-ray discussions in Chaps. 3 and 5.

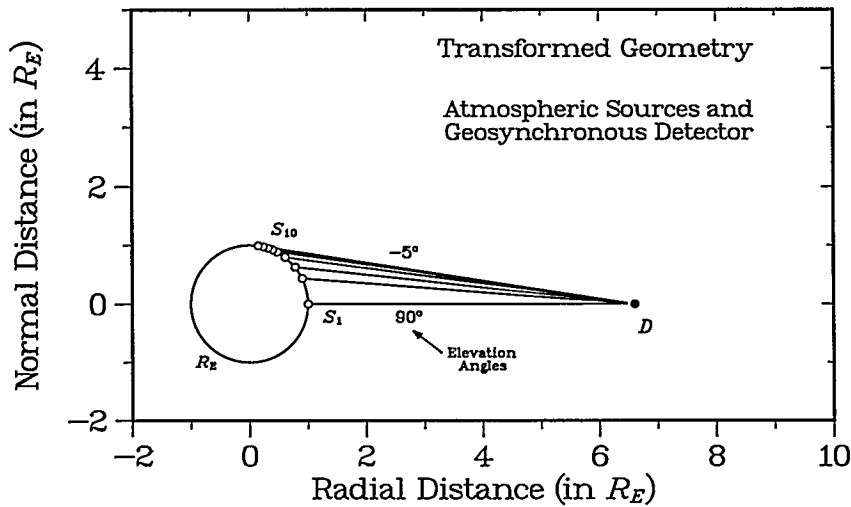


**Fig. 2.3a.** The result of transforming Fig. 2.1 to show the relationship between a geosynchronous detector and sources at different central angles.

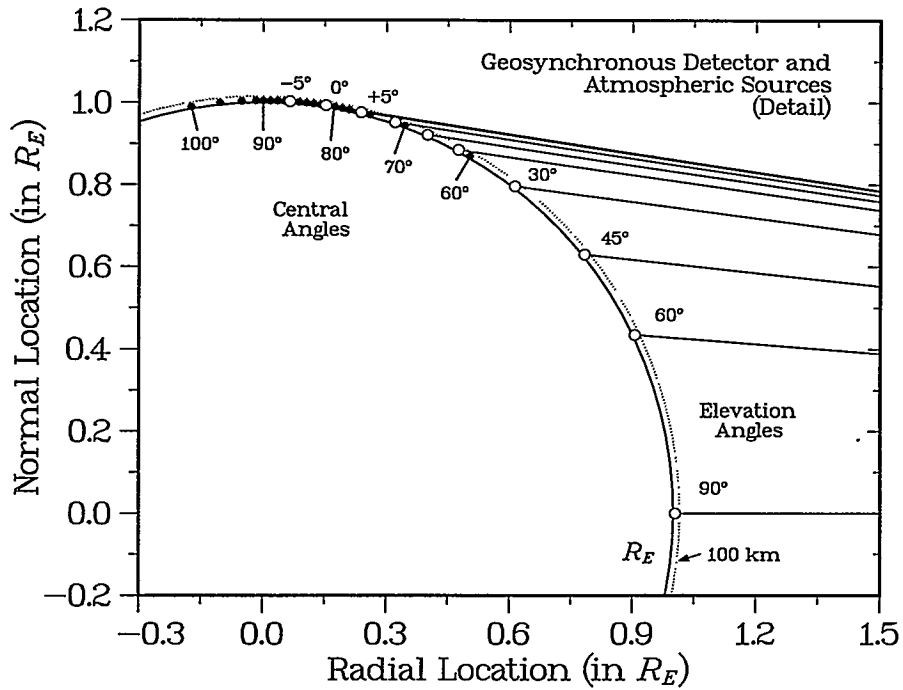


Fig. 2.3b. Enlarged geometry of Fig. 2.3a, emphasizing the connection between source locations, central angles, and elevation angles for a geosynchronous detector orbit. The open circles are sources from Ref. 1 at elevation angles down to  $\theta = -5^\circ$ ; the closed circles are sources from the present work at central angles  $\beta = 60^\circ$  to  $100^\circ$ .

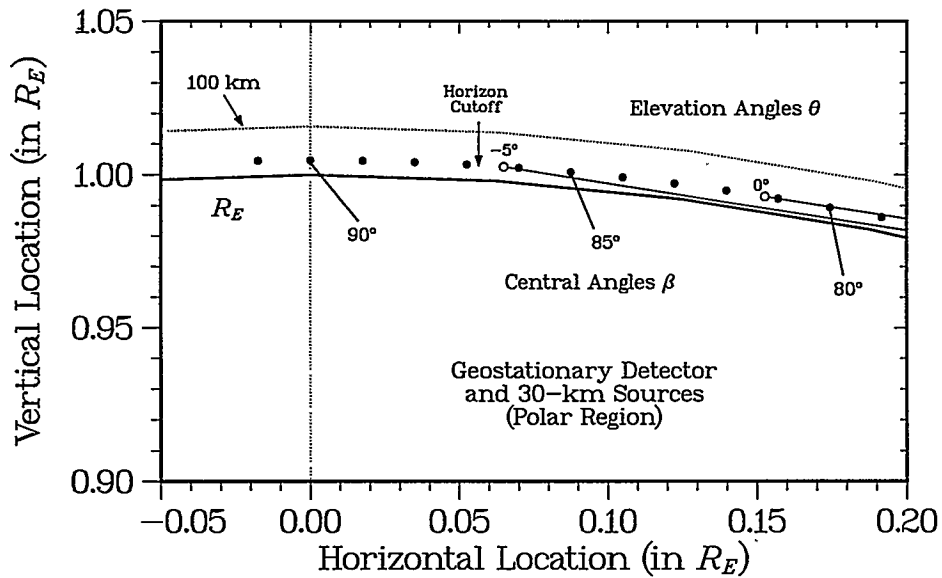


Fig. 2.3c. Geometry as in Fig. 2.3b, but expanded and relabeled for the specific case of a geostationary detector orbit with sources approaching and passing over the horizon near the Earth's geographic pole.

Table 2.2. Transformation of Central Angle  $\beta$  to Elevation Angle  $\theta$ .

Index	Central Angle $\beta$	Elevation Angle $\theta$
1	60	21.9
2	70	11.4
3	75	6.3
4	78	3.3
5	79	2.3
6	80	1.3
7	81	0.3
8	82	-0.7
9	83	-1.7
10	84	-2.7
11	85	-3.7
12	86	-4.7
13	87	-5.7
14	88	-6.7
15	89	-7.7
16	90	-8.6
17	91	-9.6
18	93	-11.6
19	96	-14.5
20	100	-18.3

**Near-Horizon Relationships.** Although our calculations apply to a detector in any geosynchronous orbit, it is convenient to consider the particular case of a geostationary orbit at the equator with sources that approach one of the Earth's poles along a meridian. Figure 2.3c shows an extreme closeup of the horizon region for a source altitude of 30 km. Again, the open circles and connecting rays are the angles from the previous report; the lowest elevation angles at  $0^\circ$  and  $-5^\circ$  correspond to central angles, in this case latitudes, at  $81.3^\circ$  and  $86.3^\circ$ . The solid circles are central angles from the present work, which extend up to and beyond the pole. Also shown is the horizon cutoff at  $\theta = -5.6^\circ$  or  $\beta = 86.9^\circ$ , which is the last angle for which a direct line of sight exists between the source and detector. The relationships would be the same for the more general, nonpolar case of a geosynchronous detector with sources approaching the horizon from any direction.

**Angular Relations.** The above figures introduce the interrelated behavior of decreasing elevation angles, increasing central angles, and varying cutoff angles. The cutoffs are calculated as

$$\theta_c = \arctan \left( R_E / \sqrt{R_S^2 - R_E^2} \right) - \frac{\pi}{2}, \quad (2.2)$$

where again  $R_S = R_E + A_S$ . The complete relationship between elevation angles  $\theta$ , central angles  $\beta$ , and cutoff angles  $\theta_c$  in the near-horizon region is shown in Fig. 2.4. Also shown is a linear approximation for the inverse conversion,  $\theta \cong 81.4^\circ - \beta$ , which is optimized for this region. A similar equation,  $\theta \cong 90^\circ - 1.11\beta$ , is less precise at the extreme angles but remains accurate to within a few degrees over the full range from  $\beta = 0^\circ$  to  $90^\circ$ .

**Discussion.** The two important results from our discussion of the calculation geometry are (1) the transformation from single-source to single-detector orientations and (2) the resulting relationships between elevation angles, central angles, and horizon cutoffs. In general, central angles are useful for understanding the source's position relative to the Earth's curvature, while elevation angles help in visualizing the inclination of the

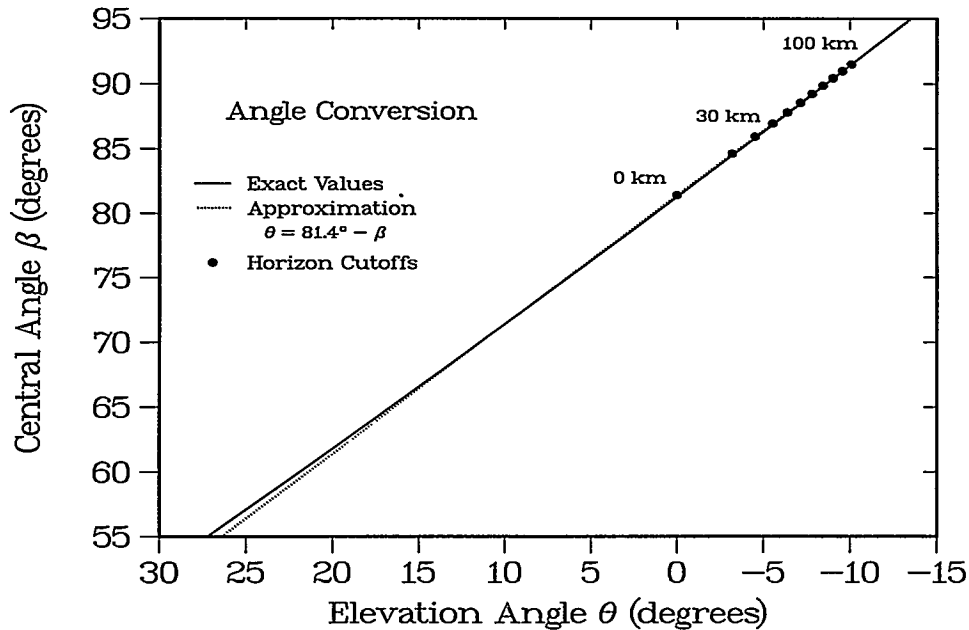


Fig. 2.4. Examination of the different angles in the near-horizon region. The  $x$ -axis gives the elevation angle  $\theta$ ; the  $y$ -axis gives the central angle  $\beta$ , and the plotted points show the horizon cutoffs for different source altitudes. The solid curve gives the true connection between the  $\beta$  and  $\theta$  values, and the dotted line shows a linear approximation.

path through the atmosphere. Accordingly, many of our figures will include both scales. Although the cutoff angles provide a simple optical observation limit, the effect of the exponential atmosphere modifies this limit dramatically, as laid out in the next section.

## 2.2. MODEL ATMOSPHERE

**General MCNP Behavior.** In the calculations for Ref. 1, the only variance-reduction technique was the use of ring-detector tallies to improve the statistical precision. This technique is also used in the present work. To exploit the problem's cylindrical symmetry, the detectors are replaced by rings at different central angles. After each collision, the average attenuation for a virtual particle travelling between the collision point and each ring is calculated, and the detector tallies are increased by the products of these transmissions and the current particle weight. The real particle is then followed to its next collision, and the process is repeated. This approach works well except for detectors near the horizon, where the probability of following a path low through the atmosphere becomes smaller than that for scattering upward and over the horizon to reach the detector. Because relatively few particles naturally follow this trajectory, the uncertainties on these tallies are usually large. To improve their statistical precision, MCNP provides additional biasing techniques that increase the sampling frequency in important regions (splitting) and decrease the frequency in less important regions (roulette). Inspection of our output files shows that additional upward-going particles are indeed created, whereas some downward-going particles are "killed off" and not followed to lower altitudes. Even with this biasing, in an exponential atmosphere most of the collisions occur below the source, although all or most of the particles that reach the detector are tracked from collision points located above the source. Only for the largest elevation angles (the most vertical

detectors) is there a significant fluence travelling through the atmosphere along the path directly between the source and the detector.

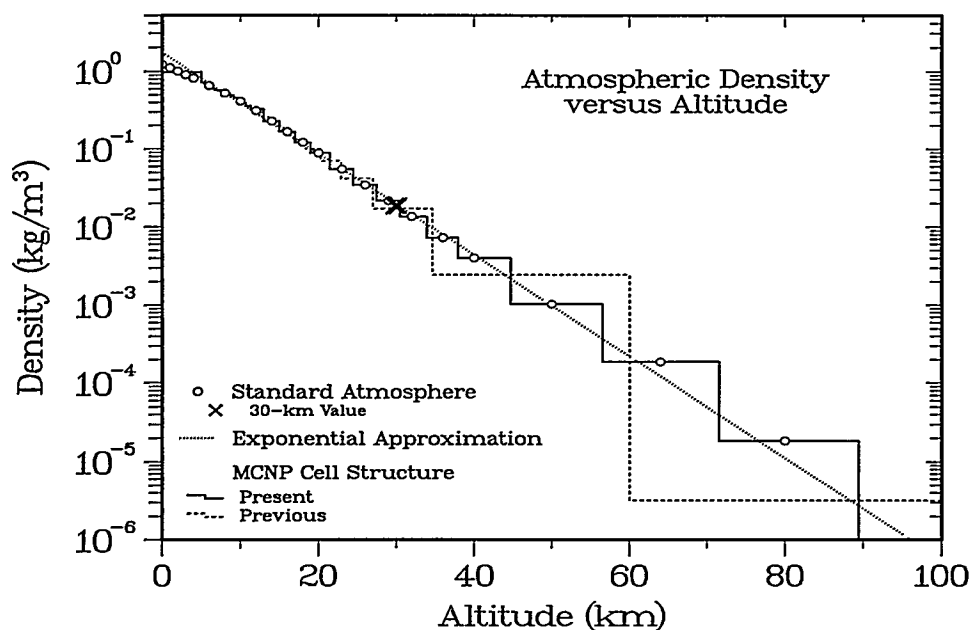


Fig. 2.5a. Atmospheric density for the present calculations, comparing the previous MCNP cell structure with the smaller spacings intended to provide a better representation for the near-horizon transport in the present report.

**Revised Atmosphere.** A recommendation in our previous study was that any subsequent work consider the use of finer graduations in the MCNP representation of the Earth's upper atmosphere. This modification is particularly important for the near-horizon case. To illustrate, Fig. 2.5a compares the altitude dependence of the present and previous MCNP cell structures with the densities from the standard atmosphere model<sup>2</sup> and an exponential approximation.<sup>1</sup> The previous altitude boundaries were adapted from those developed for earlier MCNP calculations,<sup>4</sup> which used cell sizes appropriate for vertical transport from sources deep in the atmosphere. Accordingly, the total integrated depth was carefully constrained as in Fig. 2.5b, which shows that the MCNP integrals closely follow those obtained for the standard atmosphere. In the previous study, the cell sizes were simply set to be 100 times the typical interaction distance, which is important for providing stable weighting in the variance reduction. The relevant altitude dependences of the interaction distances for gamma rays and neutrons are shown in Figs. 2.6a,b. For the gamma-ray case in Fig. 2.6a, the distance is expressed either as the microscopic mean free path obtained from the MCNP calculations or as the macroscopic interaction length for a  $1/e$  attenuation of the energy fluence, which can be calculated using the Storm and Israel ("S&I") total interaction probabilities<sup>5</sup> discussed in Sec. 2.3. For the S&I values, the different points at each altitude correspond to different elevation angles. For the MCNP results, the different values come from annular cells at increasing radii from the Earth-to-source axis, as discussed in Ref. 4. The major reason for the differences between the two approaches, as well as for the overall variation, is the density dependence shown in Fig. 2.5a.

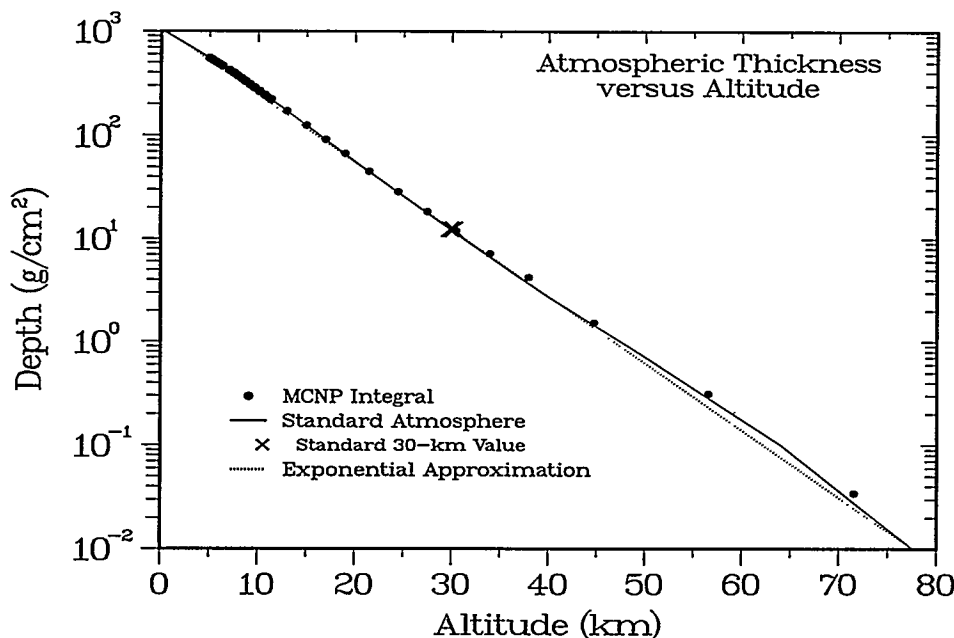


Fig. 2.5b. Atmospheric depths for the present calculations, comparing the MCNP, standard, and exponential values.

For the neutron case in Fig. 2.6b, the comparison is between values for fission and fusion sources, which give results similar to those for the gamma rays. At the 60–80 km altitudes that are just above our sources, the interaction distances range from a few kilometers to a few tens of kilometers, which is comparable with the MCNP cell sizes shown in Fig. 2.5a; at a 10-km altitude, the distance is only a meter or so. Partially because of the variance reduction's roulette procedure, no particles are followed below about 5 km. These issues set up a conflict between using coarse versus fine graduations in the MCNP geometry. On one hand, near the horizon there are particular combinations of altitude and angle that are especially critical for accurate calculation of the direct transmission to the detector. Also, for over-the-horizon transport the proper density dependence at high altitudes is crucial for calculations of the scattered fluence. Both issues favor fine graduations in the atmosphere. However, small cells contain few interactions, which creates convergence problems for the variance reduction needed to obtain good statistical accuracies. Thus, the high-altitude boundaries for the present work were chosen as a compromise between the constraints of the near-horizon geometry and the statistical precision needed to stabilize the variance-reduction techniques.

**Discussion.** As recommended in the previous report, we have reduced the granularity of the MCNP cell sizes at high altitudes to provide a better representation of the density variation in the upper atmosphere. However, the combination of an exponential atmosphere with the use of elevation angles near and beyond the horizon cutoff places serious constraints on the parameters for the atmospheric model. In this section, these constraints have required a balance between the finer graduations needed for the line-of-sight direct transmission versus the broader binning appropriate for the large mean free paths of the high-altitude scattering problem, especially when variance-reduction techniques are included. The analysis developed in the next section provides a valuable check on the appropriateness of the chosen cell structure.

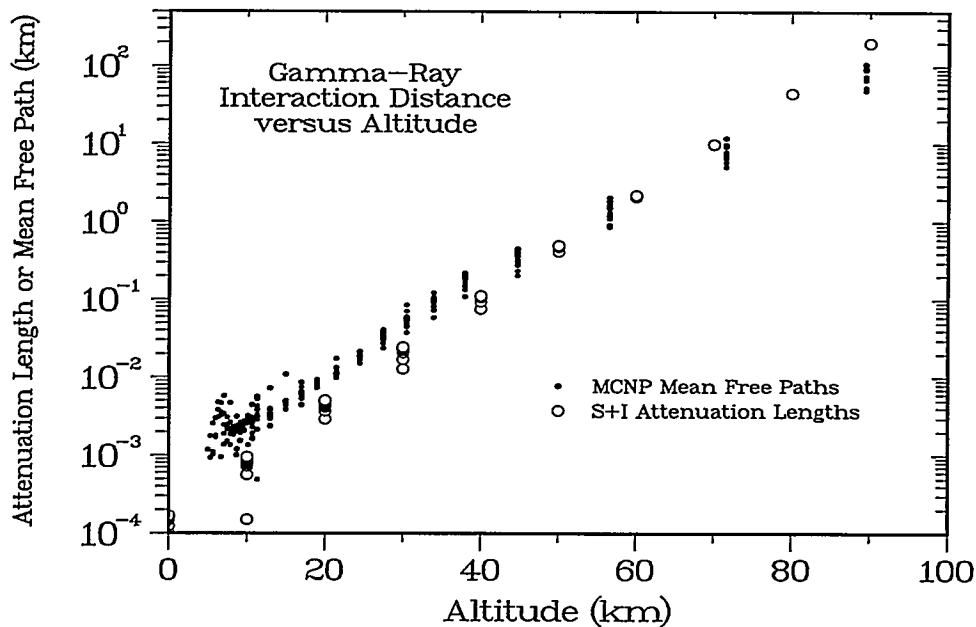


Fig. 2.6a. Altitude dependence of the typical interaction distance for gamma rays, expressed either as the microscopic mean free path or the macroscopic energy attenuation length.

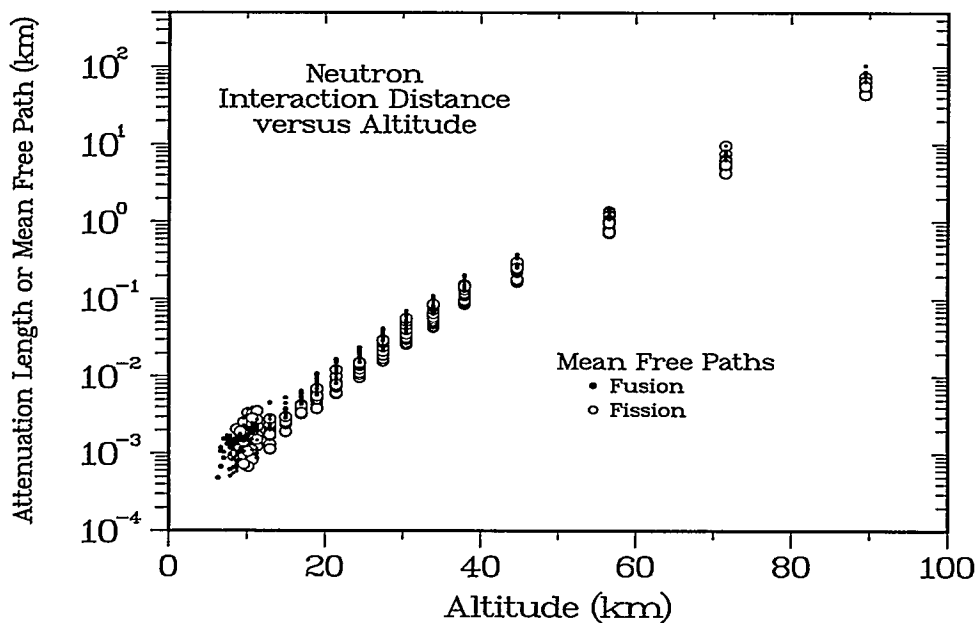
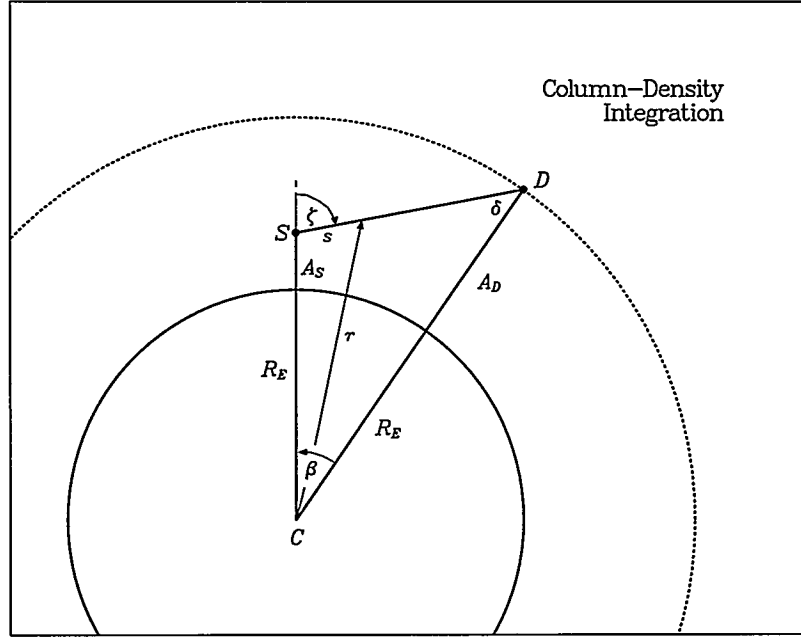


Fig. 2.6b. As in Fig. 2.6a, altitude dependence of the typical interaction distance, but for neutrons from fission and fusion sources.

### 2.3. ANALYTICAL MODEL

**Motivation.** Although non-Monte Carlo approaches to the transport problem do not provide the detail of the MCNP calculations, even a partial analytical solution would



**Fig. 2.7.** Arrangement for analytical integration of the atmospheric depth to obtain a column density.

be a valuable check on the MCNP results and might lead to simple estimates for some aspects of the problem. Such a solution can be developed by combining a calculation of the line-of-sight column density with the gamma-ray attenuation coefficients developed at LANL by Storm and Israel.<sup>5</sup> For our case, the “narrow-beam” scattering cross sections should provide a good estimate of the probability that a gamma ray reaches the detector without interacting. The absorption cross sections, however, must approximate the effect of repeated Compton scattering on the energy transport, so their results may not be accurate for the complex geometry and density variations of the near-horizon case.

**Column Density.** The first step in the analytical development is the column-density integration for the atmospheric depth between the detonation and detector. Here we refer to **Fig. 2.7**, which shows the zenith angle  $\zeta = \pi/2 - \theta$  and the distances  $r$  and  $s$  measured to an arbitrary point along the integration path. The exponential density dependence of the atmosphere is expressed as  $\rho(a) = \rho_o \exp(-a/A_o)$ , with  $a = r - R_E$  giving the altitude above the surface. In Ref. 1 we obtained the fitted values  $\rho_o = 1.63 \text{ kg/m}^3$  for the density at middle altitudes and  $A_o = 6.69 \text{ km}$  for the atmosphere’s scale height. The integral for the column density  $T$  for an arbitrary altitude and angle is then

$$T = \int_0^{s(R_D)} \rho(r - R_E) ds = \rho_o \int_0^{s(R_D)} e^{(R_E - r)/A_o} ds, \quad (2.3)$$

where  $R_D = R_E + A_D$  is the detector orbit and  $s$  is given by

$$s = \sqrt{r^2 - R_S^2 \sin^2 \zeta} - R_S \cos \zeta,$$

with  $R_S = R_E + A_S$  being the source location. This integral can be computed numerically, with an upper limit corresponding to an upper atmosphere limit of 100–200 km for convenience. The results are shown in **Fig. 2.8**, which gives the depths for central angles from



0° to 100° and altitudes from 0 km to 100 km. Because of the exponential atmosphere, the dependences for different altitudes have almost the same shapes, just scaled by a factor of  $\exp(10/6.7) = 4.4$  that reflects the 6.7-km scale height of the atmosphere. In this presentation, the densities at  $\beta = 0^\circ$  correspond to the vertical depths shown in Fig. 2.5b, and the near-horizon values at the upper right indicate the improbability of significant direct transmission in these cases. The sudden increase seen at an elevation angle of 0° indicates the cutoff where the direct path intersects the Earth's surface. Similar increases exist at lower angles for the higher altitudes.

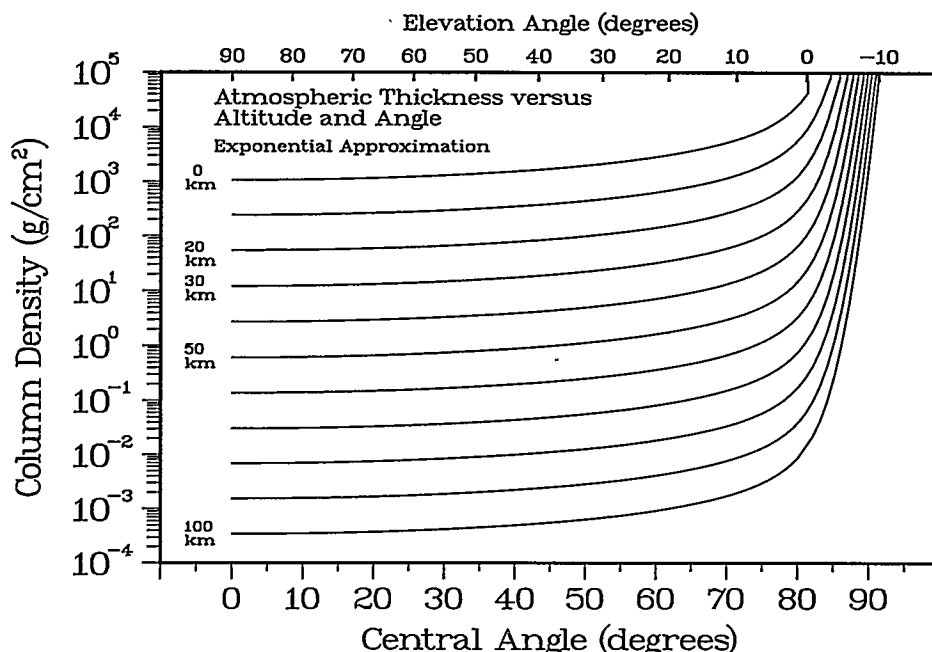


Fig. 2.8. Atmospheric depths calculated from the analytical model.

**Analytical versus Previous Attenuations.** Comparisons between energy transmissions calculated using the Monte Carlo code and those calculated using the analytical model provide a check on the assumptions in the two approaches. For MCNP, the major approximations concern the discontinuous atmospheric density and the effect of the variance reduction. For the analytical approach, the assumption of an exponential atmosphere is a slight approximation, but the major issue concerns the applicability of the S&I attenuation coefficients, which are usually associated with transport through simpler slablike shielding. These tests are more easily made with gamma rays than with neutrons, because the S&I coefficients provide a relatively straightforward way to estimate the interaction probabilities. (The corresponding neutron results will be discussed in Chap. 4.) The gamma-ray energy transmissions are shown in Fig. 2.9a, which compares the previous MCNP direct transmissions (open circles), the present MCNP results (dashed lines), and the analytical model (dotted curves). In general, the new MCNP calculations with finer atmosphere graduations agree well with the analytical results, although the previous calculations are reasonable except near the cutoff at the highest altitudes. As expected, a more detailed comparison in terms of the actual energy spectra reaching the detector shows the same behavior. A second comparison uses the fraction of the total gamma-ray energy that reaches the detector as direct fluence, which is a useful indicator of the degree

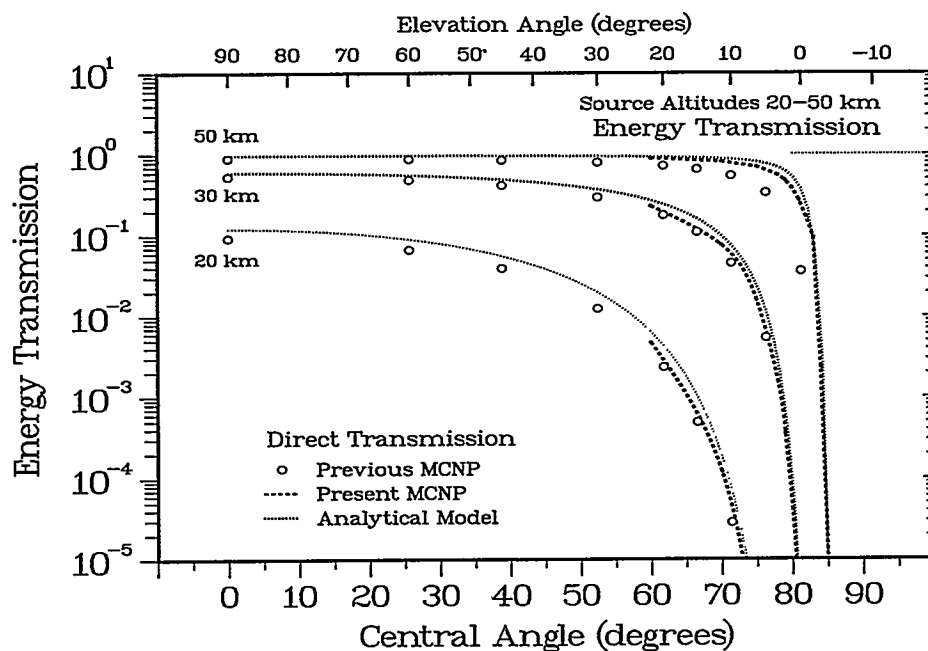


Fig. 2.9a. Comparison between energy transmissions from the present and previous MCNP calculations versus those from the analytical model.

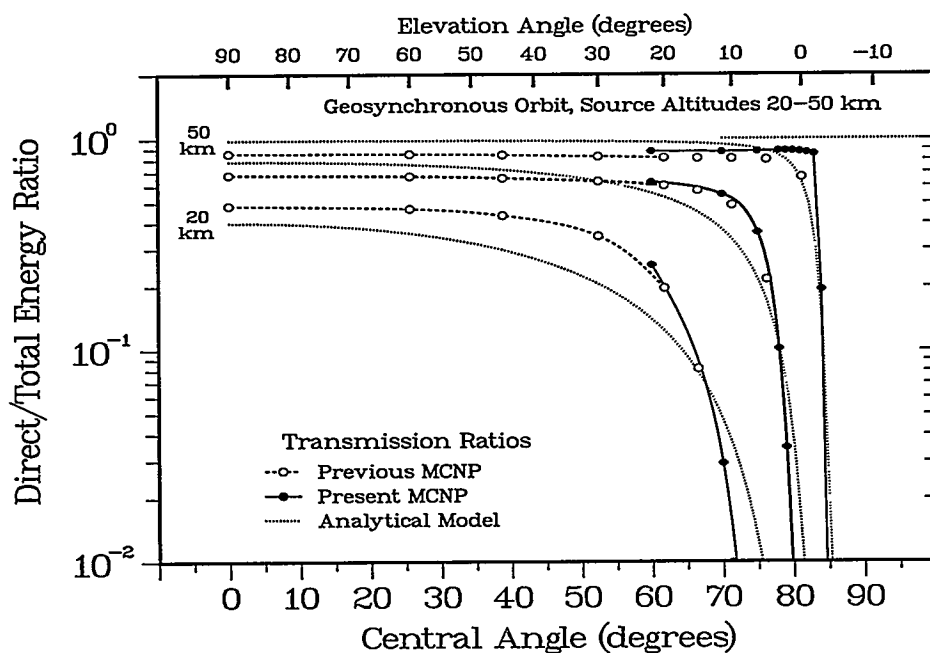


Fig. 2.9b. As in Fig. 2.9a, but for the fraction of the energy fluence that reaches the detector undistorted by atmospheric scattering.

of distortion in the original source information. Figure 2.9b shows these ratios for the three calculational approaches. The previous and present MCNP calculations are in good agreement except near the cutoff at high altitudes, where the suddenness of the present falloff again reflects the atmosphere's finer gradation and also emphasizes the narrowness

of the horizon region when viewed from a distance. In view of the agreement in Fig. 2.9a for the analytical calculations of the direct transmission, the disagreement for the ratios in Fig. 2.9b indicates that the S&I absorption coefficients can either underestimate or overestimate the scattered fluence, often seriously.

## 2.4. CALCULATION SUMMARY

**Discussion.** Although the previous study provided important insights into the transport of neutrons and gamma rays from detonations inside the atmosphere, the results immediately drew attention to the case of transport between sources and detectors at angles very close to or even beyond the local horizon. Because the MCNP code's more aggressive variance-reduction techniques were not needed at most angles and were therefore not employed, the statistical accuracy at near-horizon angles was seriously limited. In this study we have taken the complementary approach: powerful biasing techniques are used, but the study is restricted to the angular range where such techniques are necessary. In addition, the particular alignment of these cases has led to a reformulation of the source-and-detector geometry, with the traditional MCNP arrangement of a single source with multiple detectors being replaced by an equivalent layout with a single detector and multiple sources. Although this arrangement is adaptable to a wide variety of geosynchronous orbits, it is particularly relevant for the case of a geostationary detector in an equatorial orbit viewing detonations that occur at the very high latitudes of the Earth's polar regions. Our discussion of the coupling between the geometry constraints and the exponential atmosphere emphasizes the difficulty of calculations in this region, which require much more care than the relatively straightforward calculations possible at more vertical angles. Nevertheless, the comparison between the Monte Carlo and analytical results suggests that the previous calculations remain valid in all except the most extreme cases. The range of the transmission values is emphasized by Fig. 2.10, which shows the complete set of direct transmissions calculated using the analytical model. Except for the approximation of an exactly exponential atmosphere, these values should provide accurate estimates for the important unscattered portion of the gamma-ray signal. The scattered portion, however, requires the full power of the Monte Carlo approach, as discussed in the next chapter.

## 3. GAMMA-RAY TRANSPORT

**Overview.** The previous study<sup>1</sup> established a framework for presenting our gamma-ray results. Because the detectors typically measure energy fluences, not individual photons, the analyses are carried out in these terms. First, we present the altitude and angle dependence of the energy fluences in the near-horizon region. By integrating over the photon energy at the detector and then normalizing to the corresponding integrals for the same source as observed in free space, the results can be presented as transmissions for either the total fluence or only the scattered versus unscattered portions. To allow these results to be used for detectors with different energy responses, we also present the original energy spectra for several central angles at the three source altitudes. We close with a detailed discussion of the time dependence of the energy flux at the detector as a function of angle and altitude. In this area the present report goes into far more detail than the previous study.

**Integral Energy Transmissions.** In our previous work, we found that the gamma-ray energy that reaches the detector from atmospheric sources at altitudes above 30 km

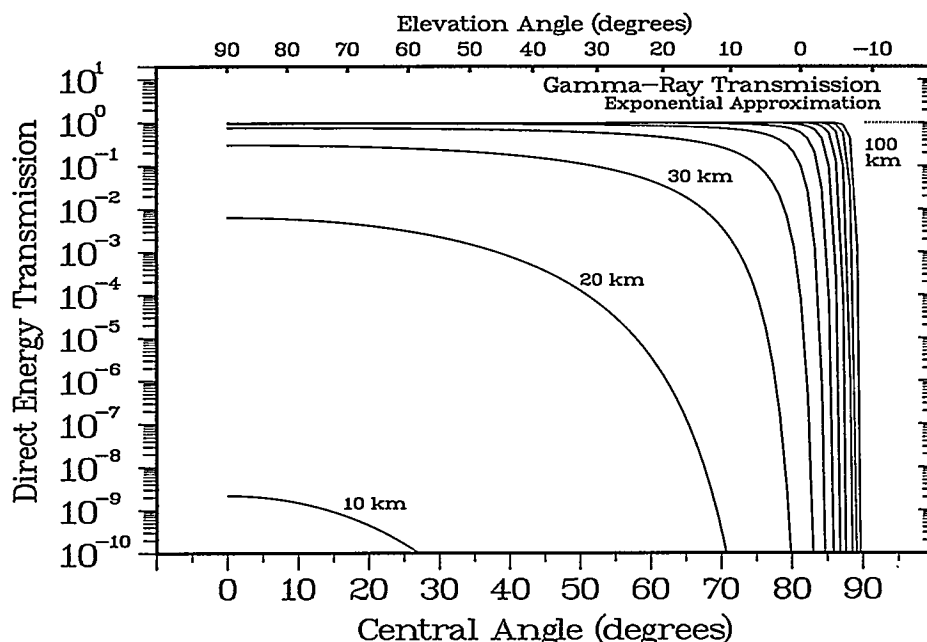


Fig. 2.10. Illustration of the broad range of gamma-ray direct energy transmissions from the analytical model.

or elevation angles above  $+5^\circ$  is at least 10% of that observed for a detonation in free space. The present work is concerned mainly with cases extending well beyond these limits. An expanded view of the direct and total transmissions in the near-horizon region is shown in Fig. 3.1a. The plotted symbols are the previous results for  $\theta \geq 0^\circ$ , with open circles for direct transmissions and closed circles for total values; the solid and dashed lines extending to the left show the trend toward more vertical angles. The heavy lines running from  $60^\circ$  toward the right show the present results. The slight discontinuities between the previous and present transmissions are a result of using a longer integration time, in the expectation that near-horizon transport may involve additional scattering delays. Except at the highest altitude, the present and previous results agree almost to the cutoff angle, which is just beyond  $85^\circ$ . Finally, the light dotted curves are the direct transmissions from the analytical model; the corresponding total transmissions are not shown because they agree very poorly. The most important aspect of the figure is the extension of the previous transmissions to angles well beyond the cutoff and the demonstration that the total transmission is nonzero throughout this region. This behavior shows that scattered gamma rays can reach the detector from sources well beyond the Earth's horizon, perhaps even at central angles near  $90^\circ$ . As the source altitude approaches 50 km, the direct fluence falls off more and more abruptly. This changing structure is mainly an effect of the direct transmission and is almost washed out in the scattered fluence, as seen in Fig. 3.1b, which shows the scattered transmissions calculated from the difference between the total and direct values. Because of the differences between the integration ranges in the two calculations, the previous results have been normalized at  $60^\circ$  and the values for the largest angles have been omitted. When viewed in this form, the energy transmission is seen to change much more slowly and to extend smoothly into the region beyond the horizon. In general, the scattered fluence decreases with depth as expected, but it also decreases at the highest altitudes because there is less atmosphere to support the scattering. The result is the complex crossover behavior shown in the figure. Not surprisingly, the analytical

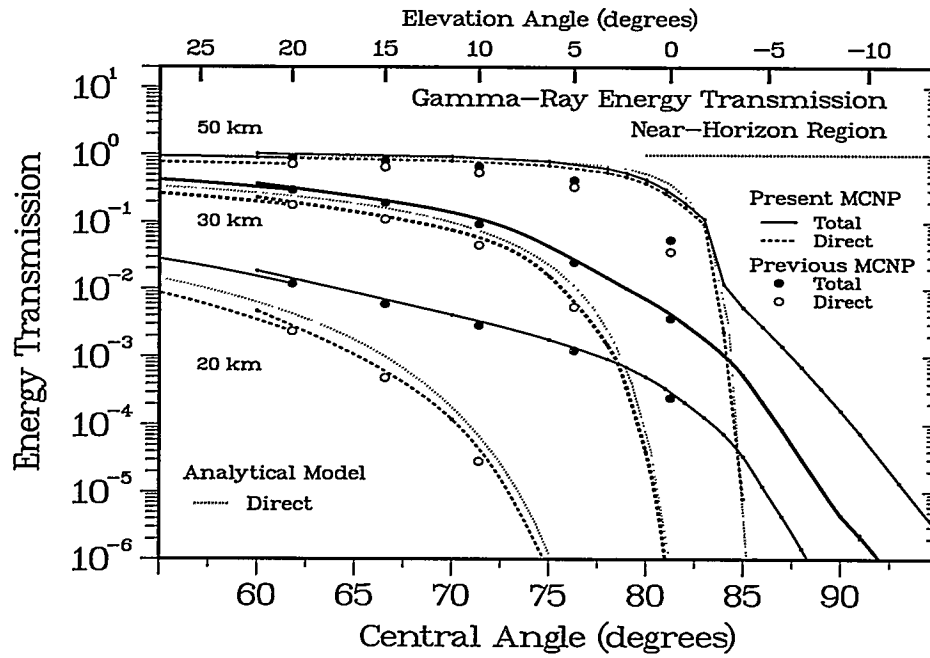


Fig. 3.1a. Angular dependence of the energy transmissions (direct and total) for sources at different altitudes, after dividing by the free-space values to obtain relative values.

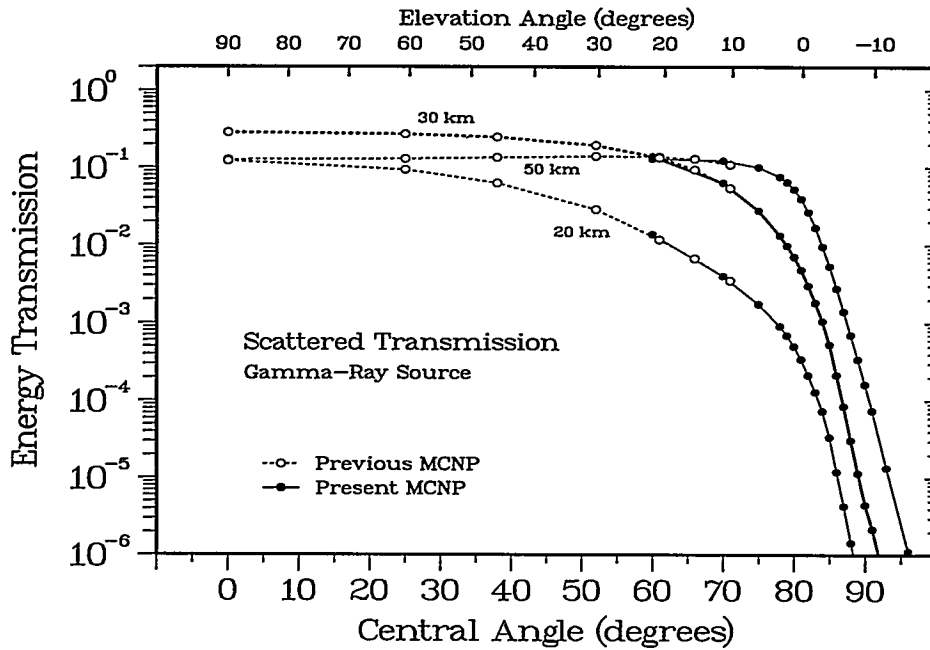


Fig. 3.1b. Altitude and angle dependence of the scattered gamma-ray transmission, as calculated from the difference between the total and direct transmission values in Fig. 3.1a.

calculations do very poorly at reproducing these features, as indicated by their failure at explaining the direct-to-total ratios in Fig. 2.9b.

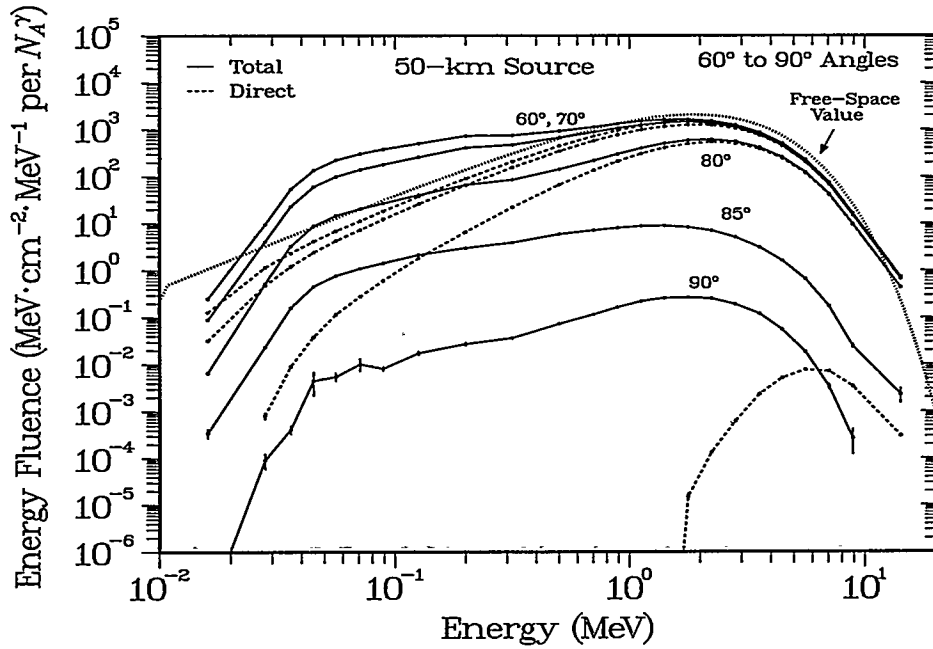


Fig. 3.2a. Energy spectra for the energy-weighted fluence from a source at 50 km incident on a detector in a geosynchronous orbit, normalized to one mole of source photons.

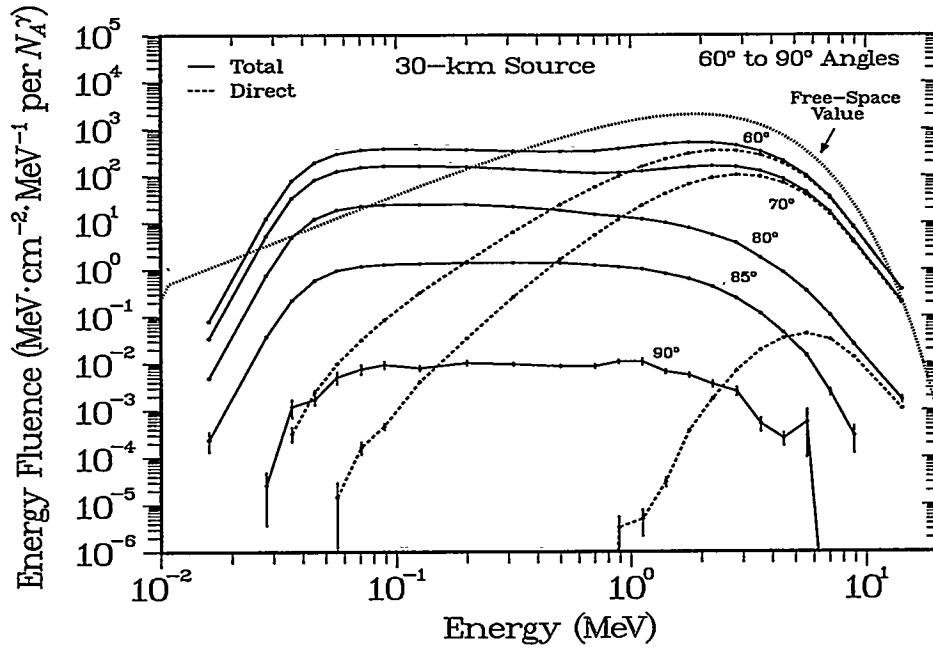


Fig. 3.2b. Energy spectra as in Fig. 3.2a, but for a source altitude of 30 km.

**Energy Spectra.** The mechanisms for energy transport at different angles and altitudes can be seen in the behavior of the energy spectra arriving at the detector. The gamma-ray source uses an MCNP evaporation spectrum, which is proportional to  $P(E) =$

$E \exp(-E/E_0)$ . The dotted curves in Figs. 3.2a–c show the free-space energy fluence, that is, the values for  $E \times P(E)$  that would be observed with no atmosphere. The other curves are the results for the total (solid) and direct (dashed) MCNP calculations. In general, the major features of the total spectrum are the underlying direct fluence at energies of 2–10 MeV and the rapid falloff caused by atmospheric absorption below 50 keV. For a given altitude, as the angle approaches the horizon the direct spectrum decreases rapidly in magnitude and its low-energy portion is gradually absorbed. Aside from the rapidly changing direct fluence, however, the total spectrum remains almost the same. As the altitude decreases, the change in the relative amounts of direct and scattered fluence causes the spectrum to spread out over angle and gradually tilt toward lower energies. This behavior is consistent with a model in which Compton interactions cause a gradual downscattering of photons to lower energies, where photoelectric absorption almost as rapidly removes them from the fluence travelling toward the detector.

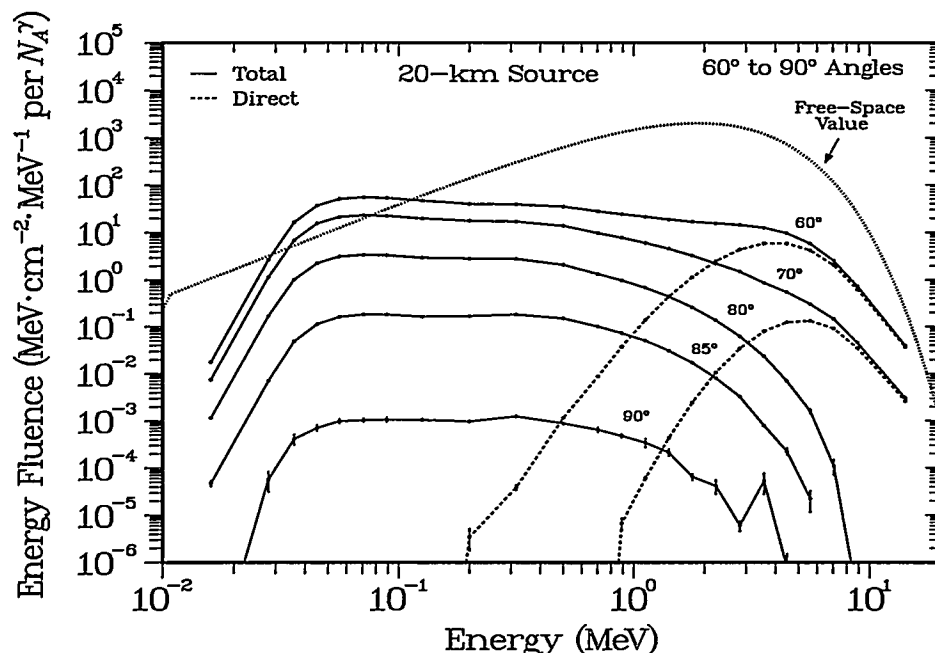


Fig. 3.2c. Energy spectra as in Fig. 3.2a, but for a source altitude of 20 km.

**Time Dependence.** For gamma-ray sources, variations in flight time are usually a simple range effect. In our case, however, the signal is modified by scattering in the atmosphere, which causes the gamma rays reaching the detector to follow longer paths and arrive at different times. Just as Figs. 3.2a–c showed the energy dependence of the fluence arriving at a geosynchronous detector, Fig. 3.3 shows time-of-arrival spectra for the energy fluxes. These energy and time spectra are actually the projections of the two-dimensional time-and-energy arrays that contain the MCNP tallies. Inspection of the original arrays reveals a gradual but definite decrease in mean energy at longer arrival times. This time-energy correlation is simply an effect of additional scattering, which leads to both lower energies and longer flight paths. In Fig. 3.3, the overall shift in time with increasing angle is caused by the increase in flight path seen in Fig. 2.3c. As the angle approaches the horizon, the peaks and the early portions of the spectra change with the direct flux, but the long tails have a characteristic decay time that is almost independent

of angle and altitude, a consequence of the diffusion of scattered energy throughout a large volume of the atmosphere. For the 80° case in particular, it appears that a measurement of the time dependence of the arriving energy flux could provide a distinctive signature of the angle and altitude of the detonation. This point is emphasized in Figs. 3.4a–c, which show high-resolution calculations at the earliest arrival times. In almost all cases, the arriving pulse has a rapid initial increase followed by long tails with various shapes, so that each combination of altitude and angle possesses a unique time dependence. Before this signature can be exploited to estimate a source location, however, an important issue is the design of instruments and analytical techniques that can respond to such a wide variety of signatures while still maintaining the desired rejection of events produced by natural backgrounds.

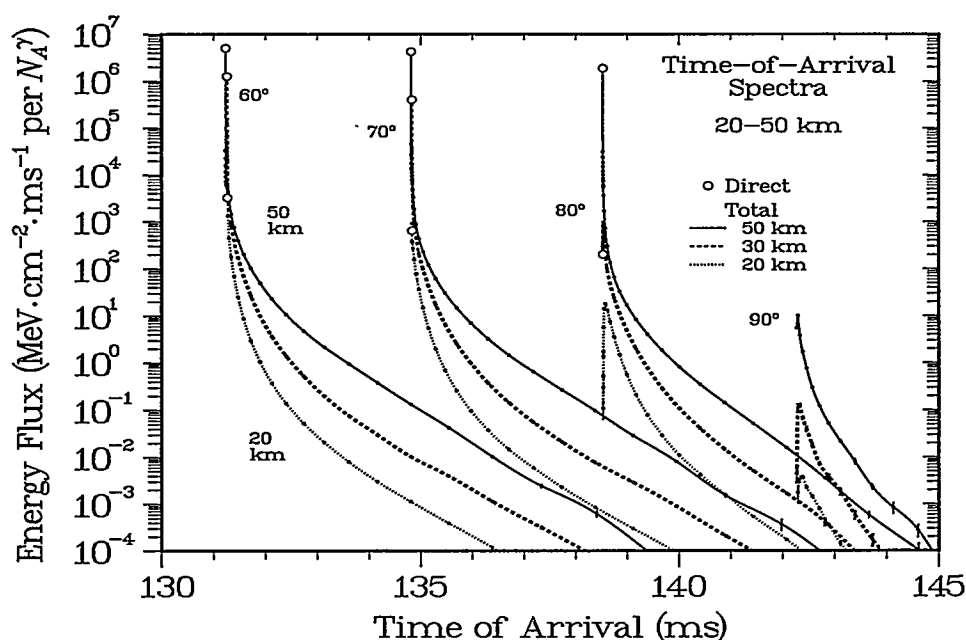


Fig. 3.3. Time dependence of the gamma-ray energy flux from sources at central angles of 60°–90° and altitudes of 50, 30, and 20 km incident on a detector in a geosynchronous orbit, normalized to one mole of source photons.

**Summary.** Much of our discussion of gamma-ray results was presaged by the comparisons in the previous chapter between the results of the Monte Carlo and analytical approaches. Most important, the present results overlap well with the previous MCNP calculations except at angles beyond the cutoff point, and the present Monte Carlo and analytical calculations are in good agreement for the direct transmissions. Beyond the cutoff angle, however, only the present MCNP calculations are valid because of the changes made in the density of the atmosphere at high altitudes. In this region, the underlying energy spectra consist mainly of lower-energy photons, but their behavior is a reasonable extrapolation of the spectra at more vertical angles. The time-of-arrival spectra at short times, however, reveal large variations with angle and altitude, a reflection of changes in the direct fluence. At long times, the similarity in decay behavior suggests a source-independent diffusion of scattered gamma rays in the upper atmosphere, where interaction distances



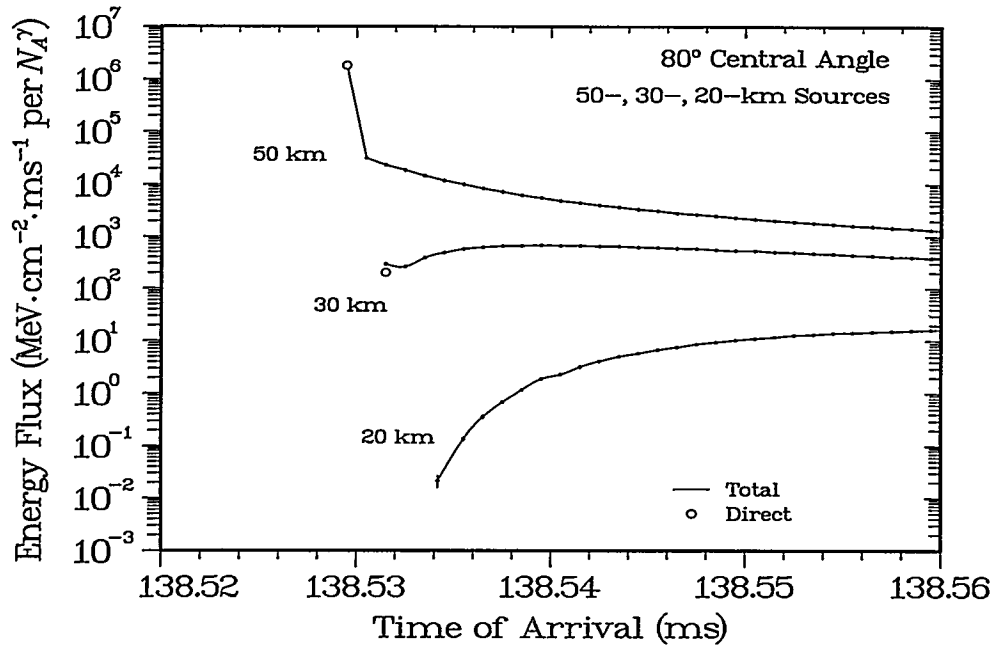


Fig. 3.4a. Expanded view of Fig. 3.3 for sources at a central angle of 80°, showing only the earliest arrival times.

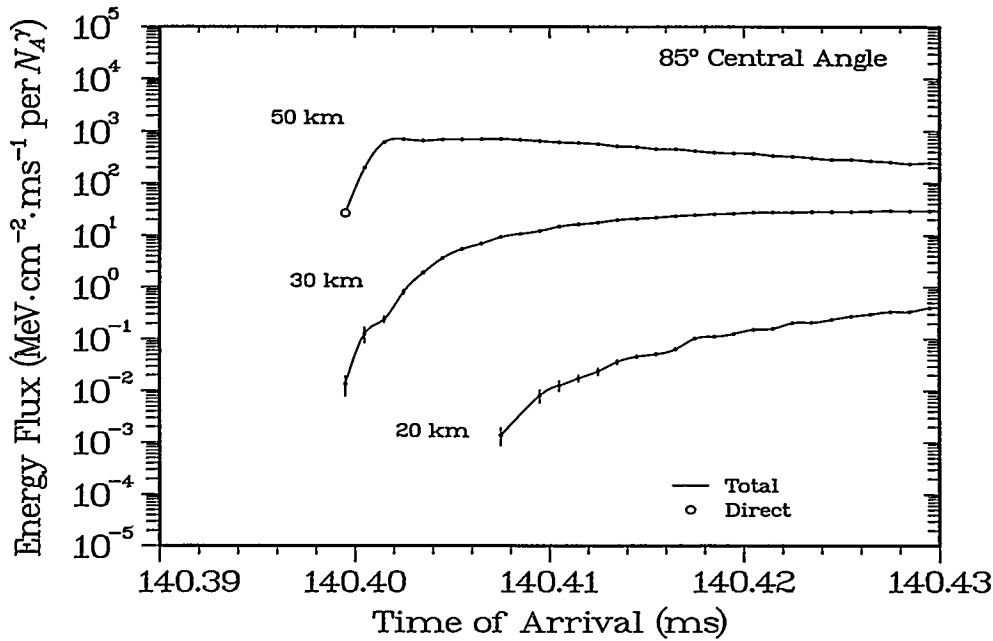


Fig. 3.4b. Early time dependence from Fig. 3.3 for sources at a central angle of 85°.

become very large. If measurable, such time spectra may provide a useful indicator for different source locations.

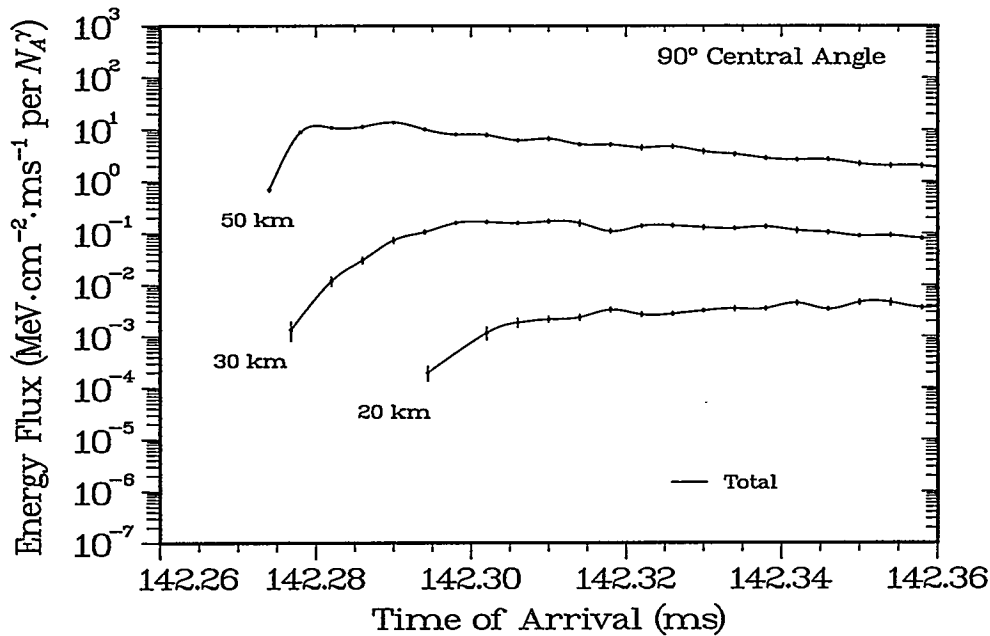


Fig. 3.4c. Early time dependence from Fig. 3.3 for sources at 90°. Note the larger range for the time scale.

#### 4. NEUTRON CALCULATIONS

**Overview.** Our gamma-ray discussion sets the stage for the corresponding neutron analyses. Because scattering should be more important in the neutron case, the changes in the atmospheric model at high altitudes should have a similar effect on the direct fluence but a larger effect on the total values. Although there are no neutron coefficients that are equivalent to the Storm and Israel tables, the National Nuclear Data Center (NNDC) maintains compilations of evaluated cross sections that can be used in a similar fashion. Accordingly, this chapter opens with direct neutron transmissions calculated by both an analytical model and the MCNP code. These analyses are followed by direct, scattered, and total transmissions calculated specifically for the near-horizon case. We then discuss the assumptions behind the time-to-energy conversions and show representative energy and time-of-flight spectra for central angles of 80°, 85°, and 90°.

**Analytical versus MCNP Calculations.** Although direct transmissions are not as useful for neutrons as for gamma rays, they provide a starting point for our comparison between MCNP calculations and the analytical model. Figures 4.1a,b show the wide-ranging transmissions obtained from the analytical model for the fusion (Fig. 4.1a) and fission (Fig. 4.1b) cases. As in Ref. 1, our generic fission source is a simple Maxwell distribution, and the fusion source uses a narrow Gaussian peak. The column densities are those calculated in Chap. 2, and the cross sections are those obtained from the NNDC for nitrogen, oxygen, and argon. The agreement between the two approaches at 50, 30, and 20 km is fairly good for both source distributions. Although the fission neutrons have considerably lower energies, there is surprisingly little difference between the results for the two sources, which indicates that the two energy-averaged cross sections are very similar.

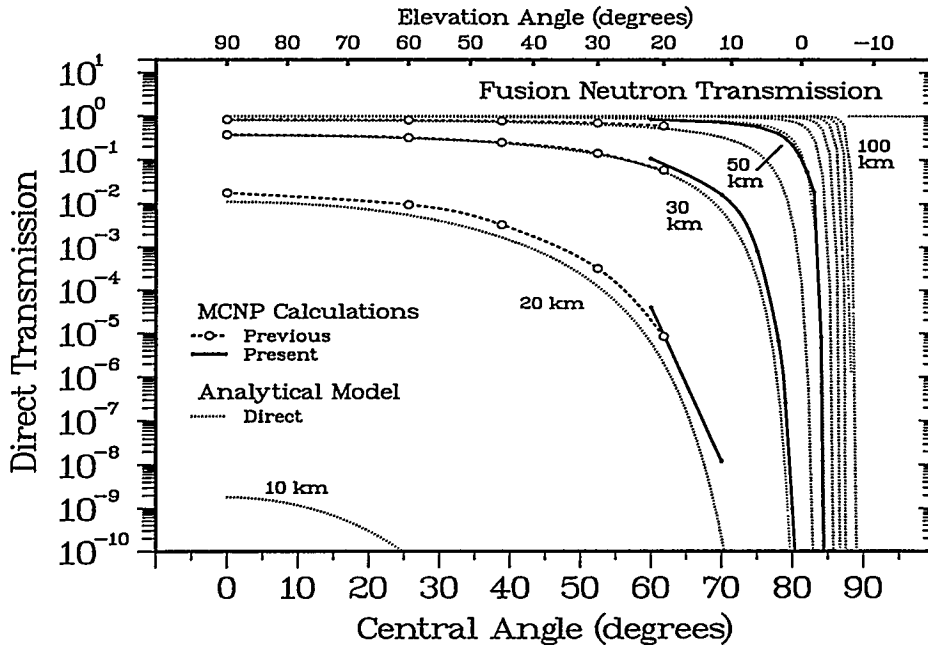


Fig. 4.1a. Angular dependence of the direct neutron fluence from fusion sources at different altitudes, as obtained from the MCNP calculations and the analytical model.

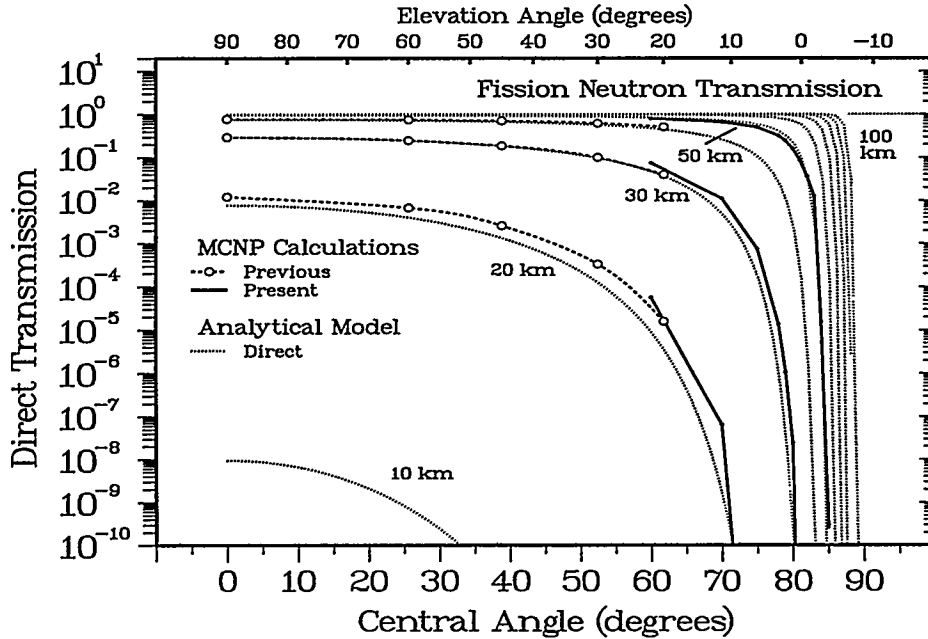


Fig. 4.1b. Angular dependences as in Fig. 4.1a, but for the fluences from fission sources.

**Direct, Total, and Scattered Transmissions.** In Figs. 4.2a,b we compare the direct and total transmissions from the present and previous MCNP calculations with the direct results from the analytical model. As in the gamma-ray analyses in Chap. 3, all

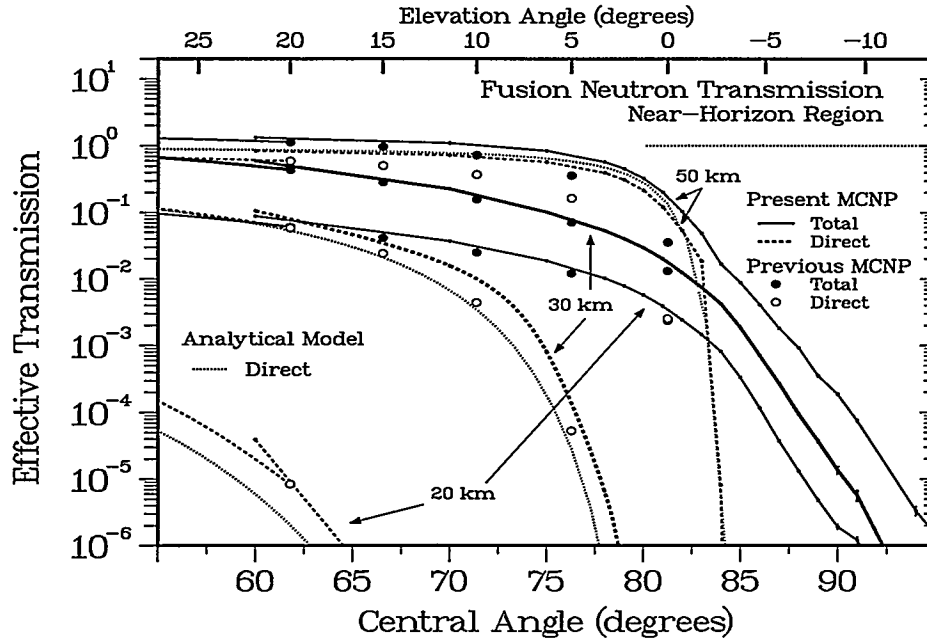


Fig. 4.2a. Angular dependence of the direct and total neutron fluences for fusion sources at different altitudes, after integration over both energy and time. The plotted symbols are the previous results, the heavy lines are the present calculations, and the dotted curves are the analytical model.

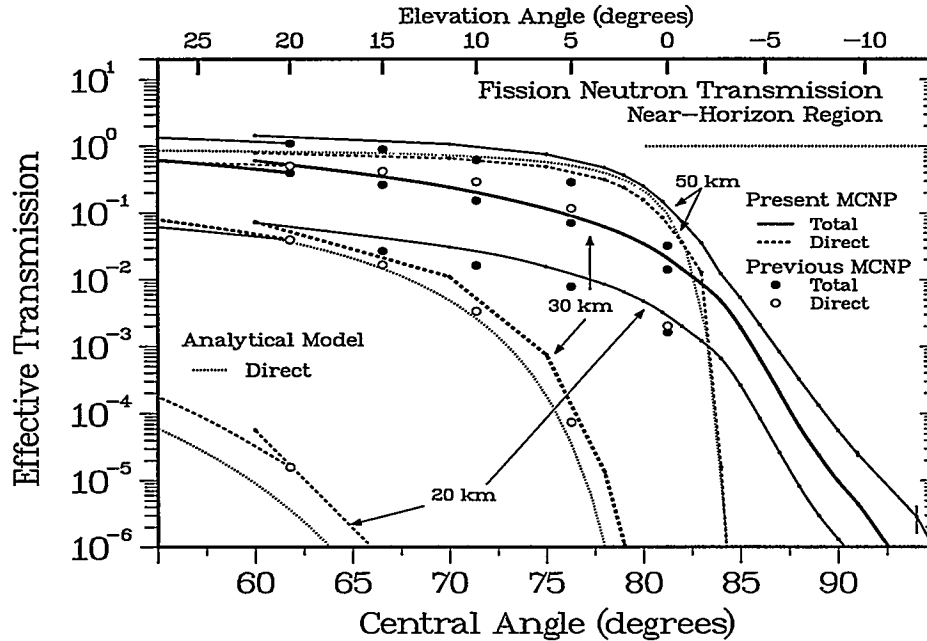


Fig. 4.2b. Angular dependence of the direct and total neutron fluences for fission sources at different altitudes, after integration over both energy and time.

transmissions are in good agreement except for the previous values at very high altitudes or at central angles beyond the cutoff value. We again assert that the major limitations in

the previous study concern the coarseness of the atmosphere binning at high altitudes. The improved granularity is most important for angles beyond the cutoff, where the present total transmissions are very different from the previous values for both the fusion and fission cases. Although evaluations of nonelastic cross sections could be used to estimate scattered or total fluences, our attempts to develop such approaches for neutrons met with even less success than those for the gamma-ray case. Certainly, no such approaches can produce transmissions greater than 1.0 at near-vertical angles, nor can they produce nonzero transmissions beyond the cutoff angle. The most useful quantity is the scattered transmission, which is again calculated from the difference between the total and direct values. As shown in Figs. 4.3a,b, the fission and fusion values are almost identical at 20 km and 30 km, but they differ considerably at the highest altitude. This result is an effect of the underlying direct transmissions, with the relatively few scatterings at high altitudes giving results that approach the direct values, while the scattering at low altitudes averages over any details of the transport. In this respect, the behavior is very similar to that seen in the corresponding gamma-ray transmissions shown in Fig. 3.1b.

**Time-to-Energy Conversion.** Although transmissions provide the basic overview needed to evaluate the usefulness of the neutron information as a function of angle and altitude, a realistic assessment requires examining the energy dependence of the neutron fluence, which is essential for deciding whether a signal results from a natural occurrence or a nuclear detonation. However, because few neutron detectors actually provide neutron energy information, analyses must instead rely on time-of-arrival measurements to determine the velocity distribution, which can be converted into a neutron energy spectrum. This process depends, of course, on there being a time-to-energy correlation in the data. For example, the above gamma-ray time-of-arrival distributions provide little energy information because they result primarily from differences in flight path, not differences in energy. For the neutron calculations in Ref. 1, we showed such a correlation for a detector in a 100-km orbit, which is repeated here in Fig. 4.4a. Although a distinct locus exists, the time-to-energy conversion differs from the free-space relationship (dotted line) because deflections from the straight source-to-detector path are coupled with both greater energy losses and longer flight times. Surprisingly, the resulting correlation is well described by a power-law relation, as indicated by the dashed line. The reason for repeating this analysis in the present report is seen in Fig. 4.4b, which shows that the current results for a geosynchronous detector apparently follow the standard relation almost exactly. The difference is the change in detector orbit, from an altitude of 100 km to almost 36 000 km. For the smaller orbit, the change in arrival time caused by scattering makes up a significant fraction of the total time of flight; at the larger distance, the change is negligible and the standard time-to-energy conversion for the path beyond the atmosphere dominates. Most important, the agreement with the standard correlation in the present case means that the energy and time-of-flight distributions can be interpreted on the same physical basis.

**Energy Spectra from Fusion Sources.** Because energy measurements are the simplest to interpret, we begin our discussion in the energy domain even though such measurements are not directly obtainable. Similarly, we also start with a hypothetical pure fusion source, whose distorted spectra in Figs. 4.5a–c emphasize the effect of atmospheric scattering on the information that is observed at the detector. These spectra show angles from 60° to 90° for three MCNP runs at altitudes of 50, 30, and 20 km. Only at the highest altitudes and angles does the direct distribution reach the detector with appreciable intensity, but in essentially all cases there remains at least a prominent high-energy shoulder, which is followed by a long tail of neutron downscattering to lower energies. The structure

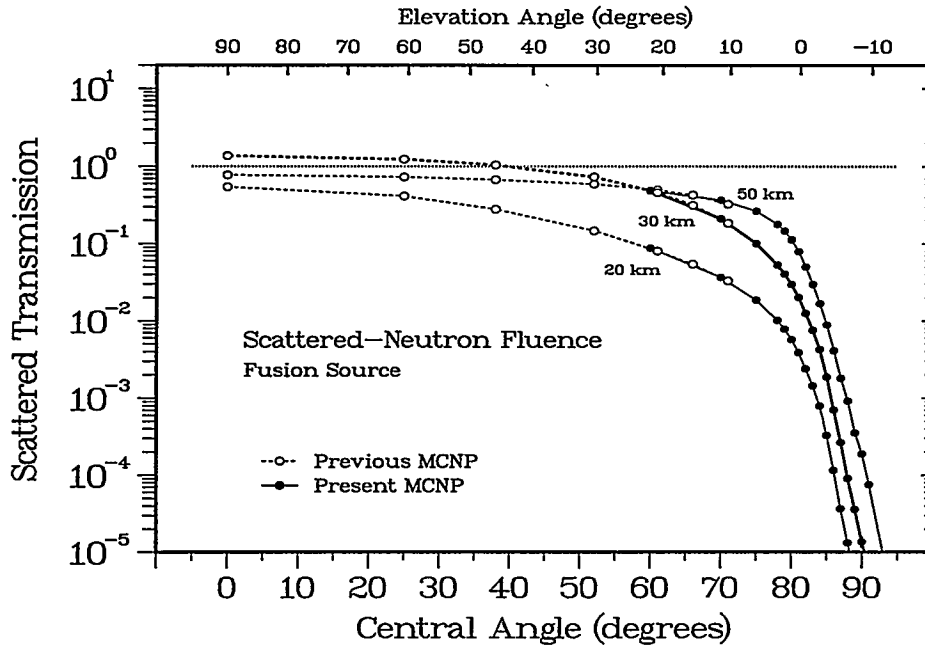


Fig. 4.3a. Angular dependence of the scattered-neutron transmissions (total minus direct) for fusion sources at different altitudes.

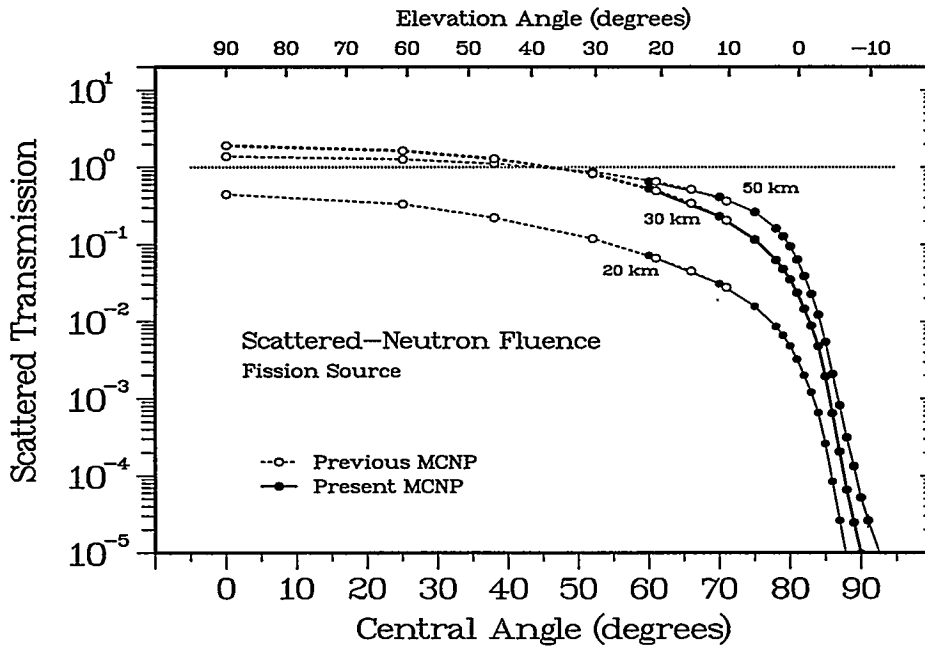


Fig. 4.3b. Angular dependence as in Fig. 4.3a, but for scattered neutrons from a fission source.

in this tail is created by resonances in the scattering and absorption cross sections for the nitrogen and oxygen that make up the bulk of the atmosphere.<sup>6</sup> In fact, calculations with finer resolution reveal even more structure,<sup>4</sup> because many of the resonances are quite narrow. The behavior shown here is qualitatively similar to that for the broader range of

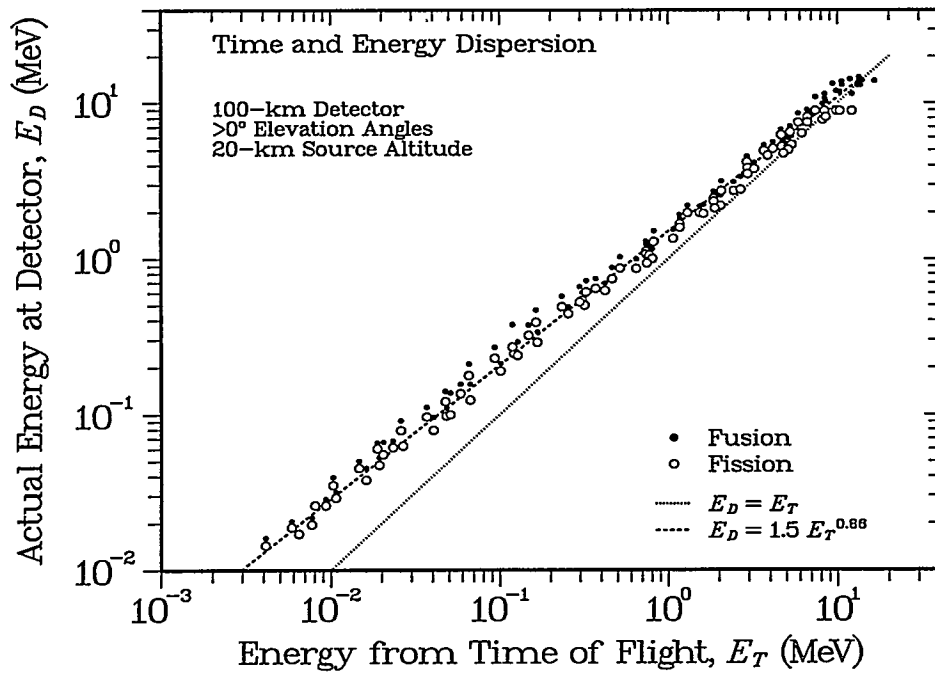


Fig. 4.4a. Locus comparing neutron energies as determined by time of flight to a detector at 100 km with the actual energies at the detector. The dotted line shows the trivial free-space relationship; the dashed line shows an empirical power law.

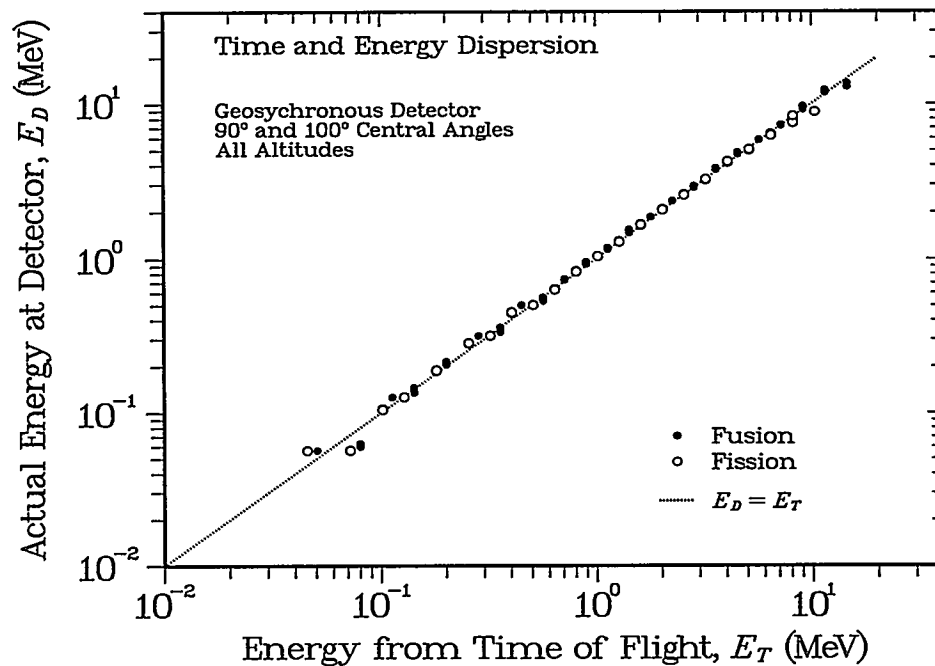


Fig. 4.4b. As in Fig. 4.4a, locus comparing actual and time-of-flight energies, but for a geosynchronous detector. The line through the data shows the trivial free-space relationship.

angles shown in Ref. 1. However, the present study includes results beyond the horizon cutoff, which accounts for the large error bars on the 90° spectra. Because of these large uncertainties, the 90° cases will be discussed separately at the end of this chapter.

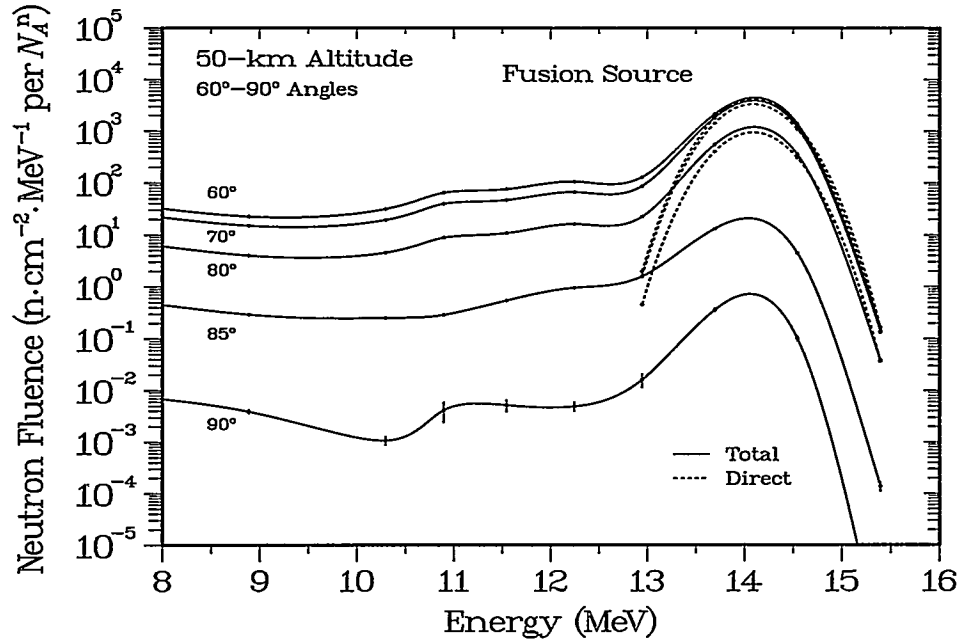


Fig. 4.5a. High-energy portions of the neutron energy spectra from fusion sources at 50 km for different angles.

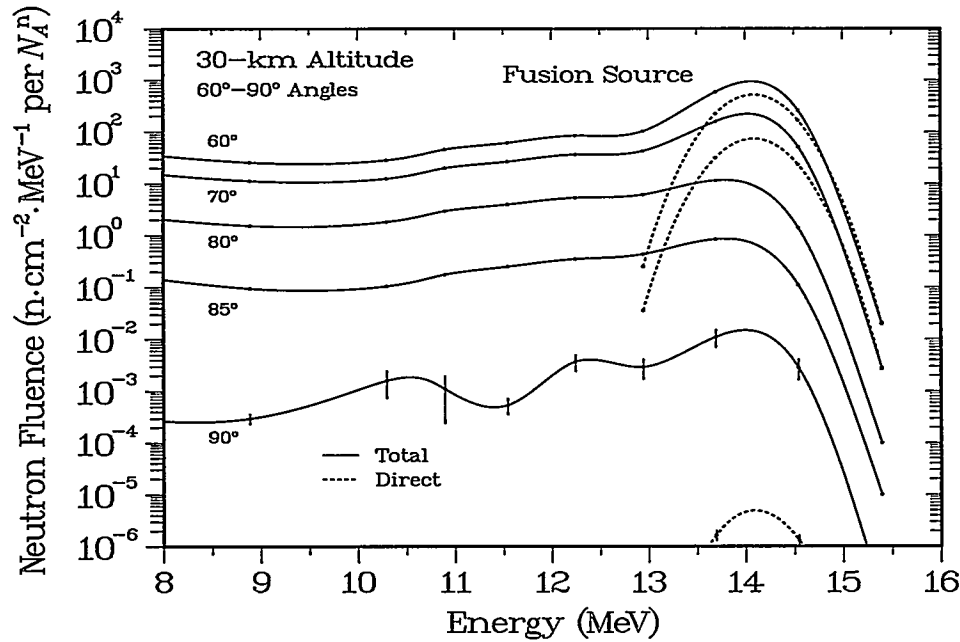


Fig. 4.5b. As in Fig. 4.5a, high-energy spectra from fusion sources, but for a 30-km altitude.



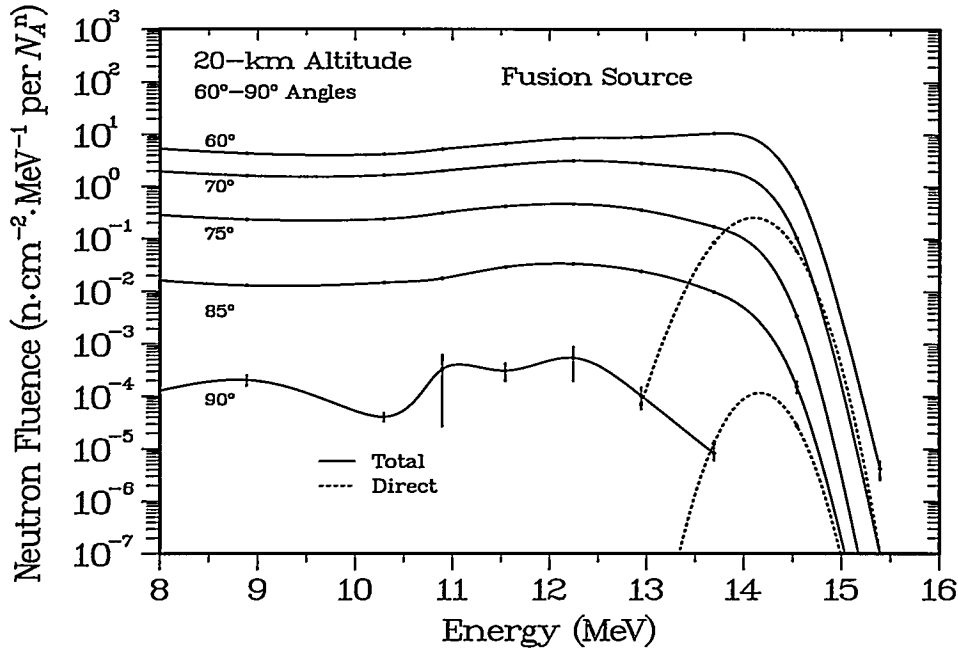


Fig. 4.5c. As in Fig. 4.5a, high-energy spectra from fusion sources at a 20-km altitude.

**Full-Range Energy Spectra.** A slightly different view of the energy dependence of the downscattered neutron fluence is seen in Figs. 4.6a,b, which show the 80° and 85° spectra over the full calculated range from 0.2 to 20 MeV. Only for 80° and 50 km is there a noticeable direct component, although a scattered reflection of the fusion peak is apparent in all cases. Note in particular that the reflected peak in the 20-km spectrum has been downshifted in energy, but it remains an identifiable feature. Again, the systematic resonance structure in the long tail is obvious, although the details at the highest energies are limited by the resolution of the MCNP calculations.

**Time-of-Flight Fusion Spectra.** In Figs. 4.7a,b we show the time-dependent version of the energy spectra in Figs. 4.6a,b. In this case we simply project the two-dimensional array of MCNP time and energy tallies onto the time-of-flight axis instead along the energy dimension. The time range matches the energy range in the previous figures, with energies of a few hundred keV corresponding to arrival times of 10–20 s. Similarly, the energy resonances at 1–10 MeV in Figs. 4.6a,b appear as the time structure at 1–3 s in Figs. 4.7a,b. Because the changing  $dE/dt$  transformation compresses the spectrum at short times and expands it at longer ones, the results are strongly peaked toward high energies and the structure is calculated with poorer resolution.

**Fission Spectra.** The fission spectra corresponding to the fusion time-of-flight results are shown in Figs. 4.8a,b for the 80° and 85° central angles. Here the high-energy time compression has the important result of transforming the essentially exponential high-energy tail of the fission energy distribution into a sharp shoulder in the time-of-flight representation. The 1-MeV peak in the original fission distribution appears as a broad continuum from 1–4 s, followed by a steady falloff similar to that seen in the fusion case. However, a very important point is the distinguishability between the fission and fusion spectra in Figs. 4.7a,b versus Figs. 4.8a,b. If an absolute reference for the time scale is available, as from the gamma-ray flash in Fig. 3.3, then the maximum energies calculated

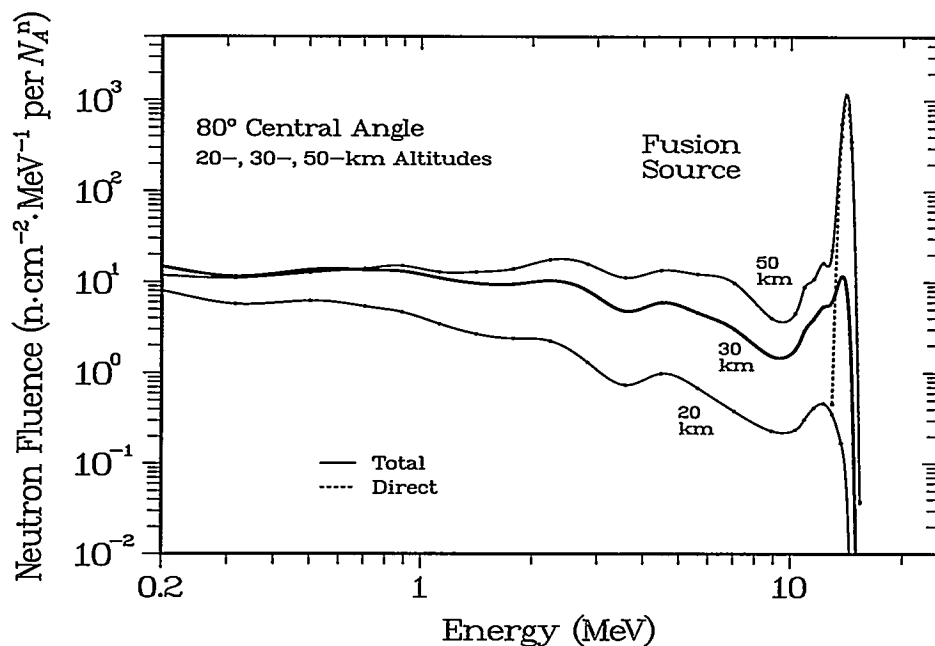


Fig. 4.6a. Altitude variations in the neutron energy spectrum from fusion sources at an 80° central angle.

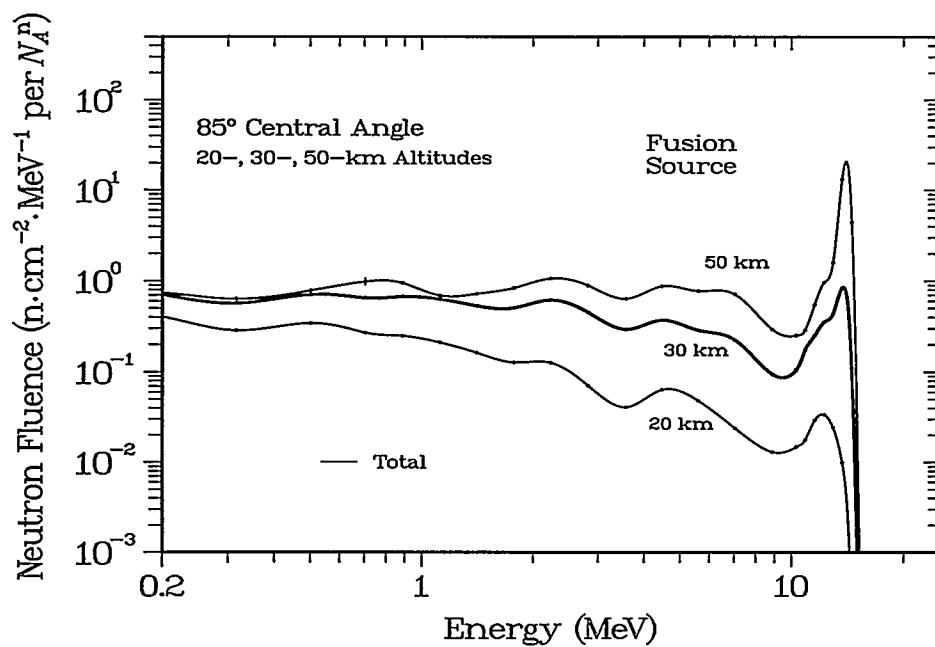


Fig. 4.6b. Altitude variations as in Fig. 4.6a, but for an 85° central angle.

for fission and fusion spectra would be distinctly different. In the realistic case of a mixed fission-fusion source, however, a shape analysis is certain to be necessary for interpreting the data.

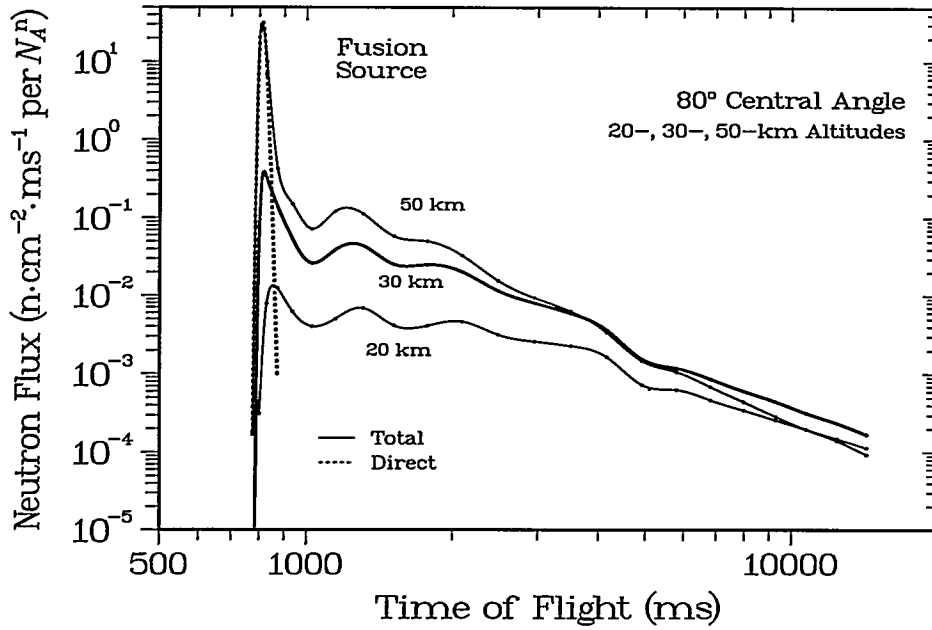


Fig. 4.7a. Altitude variations in the neutron time-of-flight spectrum from fusion sources at altitudes of 20, 30, and 50 km and an 80° angle.

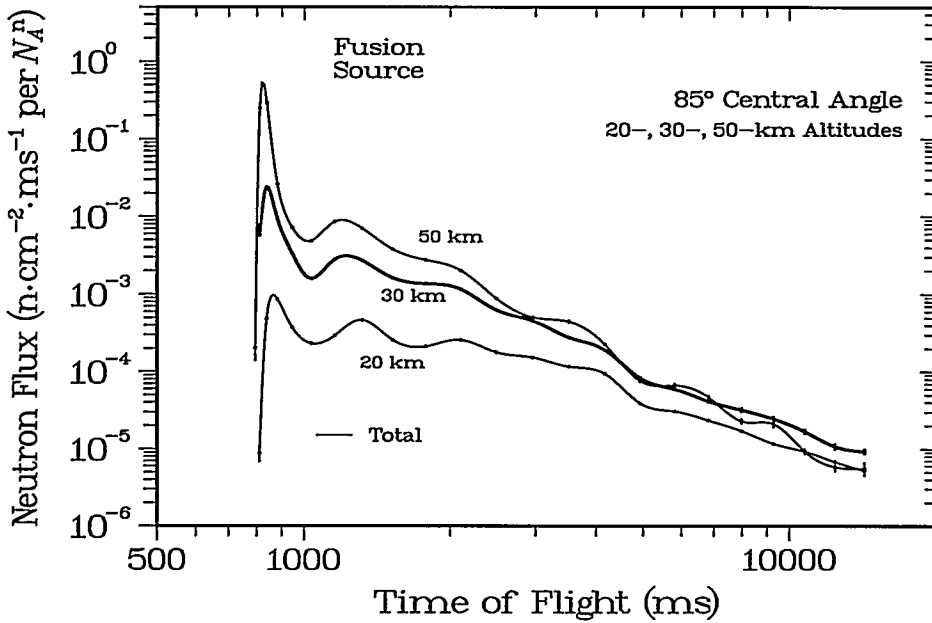


Fig. 4.7b. Altitude variations as in Fig. 4.7a, but for fusion sources at an 85° angle.

**Time-of-Flight Spectra for 90° Central Angles.** Our final figures in this chapter show calculated time-of-flight spectra for the severe case of sources at a 90° central angle, well beyond the horizon cutoff. Although the calculation could be for any direction, for orientation it is helpful to identify the particular case of a source at the Earth's North Pole

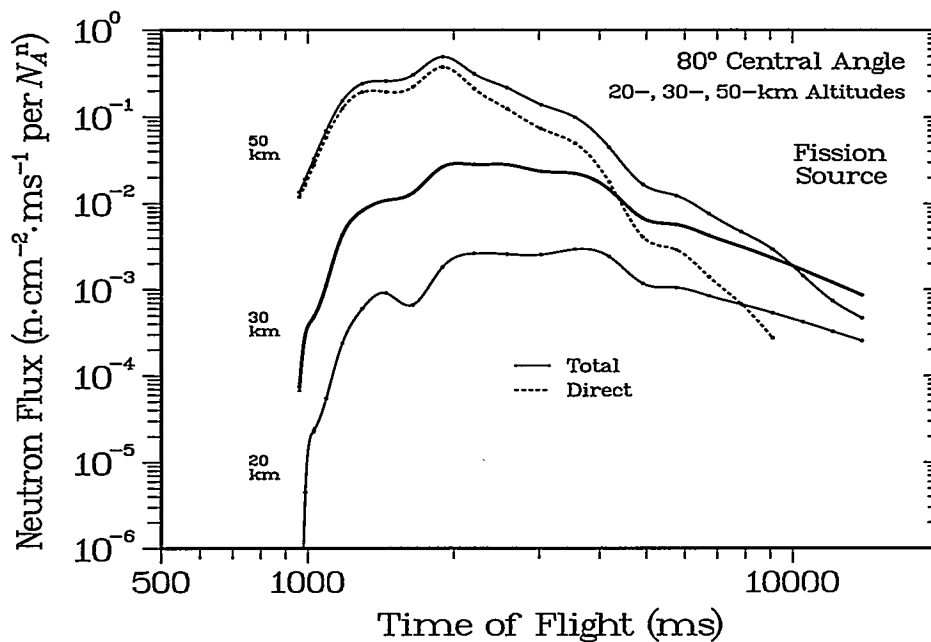


Fig. 4.8a. Altitude variations in the neutron time-of-flight spectrum from fission sources at 80° as observed at a geosynchronous detector.

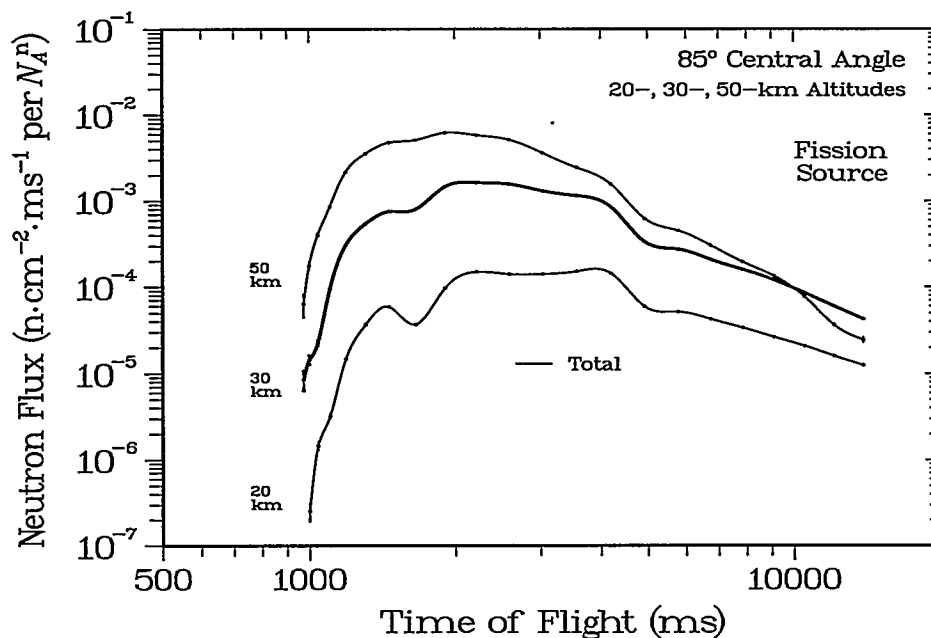


Fig. 4.8b. Altitude variations as in Fig. 4.8a, but for fission sources viewed at 85°.

and a detector in a geostationary orbit at the Earth's equator. The large error bars in Figs. 4.9a,b emphasize the difficulty of the calculations. For the fusion case (Fig. 4.9a), the high-energy peak and the nuclear resonance structure appear to be visible except at

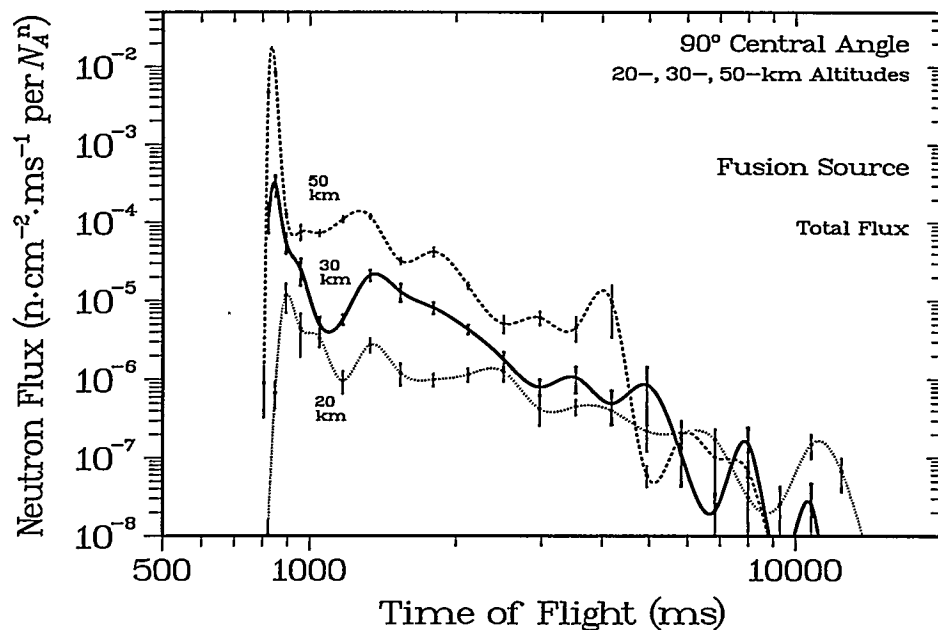


Fig. 4.9a. Altitude variations in the neutron time-of-flight spectra from fusion sources at 20, 30, and 50 km and at a 90° angle.

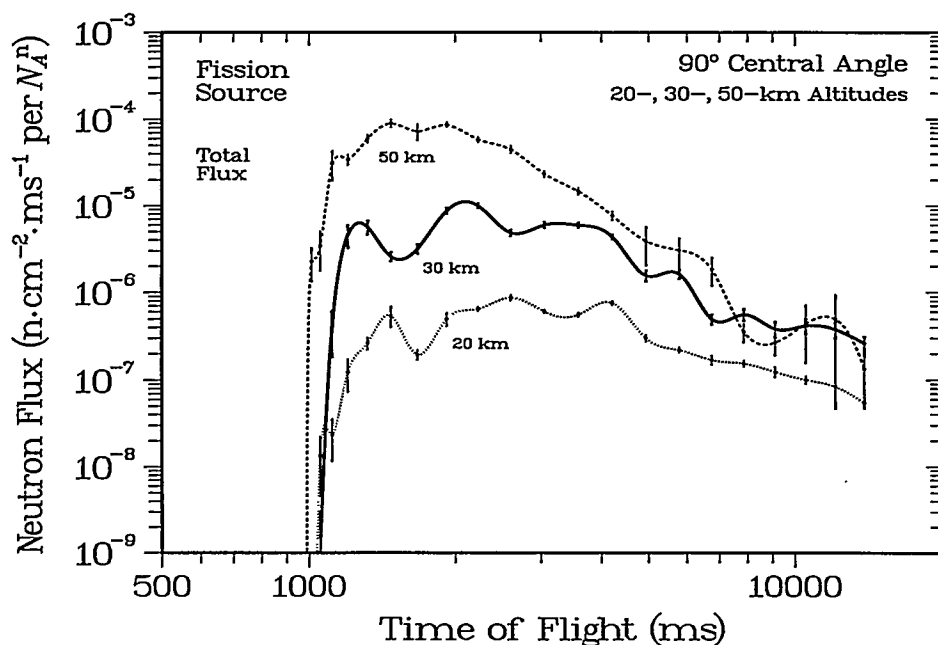


Fig. 4.9b. Altitude variations as in Fig. 4.9a, but for fission sources observed at 90°.

the lowest altitude, where the spectrum could be distinguished from natural backgrounds only by its rapid rise at the shortest times and the long duration of the elevated neutron flux. This assessment is doubly applicable to the fission spectra in Fig. 4.9b, where little of the structure appears to be physically significant. Only by its sudden rise at early

times and its correlation with other measurements could a candidate signature be reliably identified.

**Neutron Summary.** Our results in this chapter appear to be a straightforward extension of those from the previous study.<sup>1</sup> The important additions are the use of NNDC cross sections for analytical calculations, the inclusion of scattered transmissions, and the reliance on variance reduction to extend the analyses to beyond-the-horizon sources. An important result is the high-energy time compression in both the fission and fusion spectra, which creates a relatively sharp rise in flux when the source neutrons first reach the detector. If the neutron signal is to be observable in the far-horizon region, additional effort will be required to ensure the distinguishability of this signature relative to the natural background.

## 5. SECONDARY GAMMA-RAY PRODUCTION

**Overview.** An additional set of calculations was made by combining the source definitions from the neutron problem with the tally specifications for the gamma-ray case. These coupled neutron-photon calculations give the production rates of secondary gamma rays from inelastic neutron scattering in the atmosphere. The previous report described similar calculations for more vertical angles; for the present near-horizon case, variance-reduction techniques were used to improve the transport of both the source neutrons and the resulting gamma rays. For comparison with the single-channel calculations, the energy flux for the gamma rays reaching the detector is normalized per mole of source neutrons. In some cases, this secondary flux can exceed that for the original source gamma rays.

**Fusion and Fission Results.** In Figs. 5.1a,b we repeat the 50-km and 20-km time-of-arrival spectra from Fig. 3.3 for the source gamma rays, and we add the corresponding spectra for the secondary gamma rays from  $(n,n'\gamma)$  reactions in the atmosphere. First, at each angle the secondary fluxes from the fusion and fission sources have essentially the same shape, which reflects the almost energy-independent properties of neutron transport in the atmosphere, not the characteristics of the original source. In particular, the much slower rate of leakage and absorption for neutrons dominates that for gamma rays, which results in longer decay times for the secondary fluxes. Second, the magnitude of the secondary flux depends strongly on the energy of the neutron source, so fusion sources generate much larger outputs. Finally, for 50 km the source flux far exceeds the secondary fluxes at all angles, but for 20 km the fusion results at  $80^\circ$  are comparable with those for the original source. This behavior suggests that the longer decay time for the neutrons becomes a particularly important issue as the nearly direct source flux at the earliest times is cut off by the horizon.

**Near-Horizon Cases.** The comparison between source and secondary fluxes near the cutoff is examined in more detail in Figs. 5.2a,b, which show several time-of-arrival spectra at  $80^\circ$  and  $90^\circ$  with higher resolutions. At both angles, the magnitude of each set of source, fusion, and fission fluxes decreases gradually with increasing depth, with the shapes of the fusion and fission fluxes varying together and showing structure associated with the underlying resonances in the neutron time of flight. Again, once the near-direct part of the source flux is blocked at lower altitudes, the fusion flux begins to dominate, further contributing to the changing time signatures for different source locations. These changes are emphasized by the detailed  $80^\circ$  results shown in Fig. 5.3. As indicated by the vertical arrows, the slight increase in the source-to-detector distance and the occultation

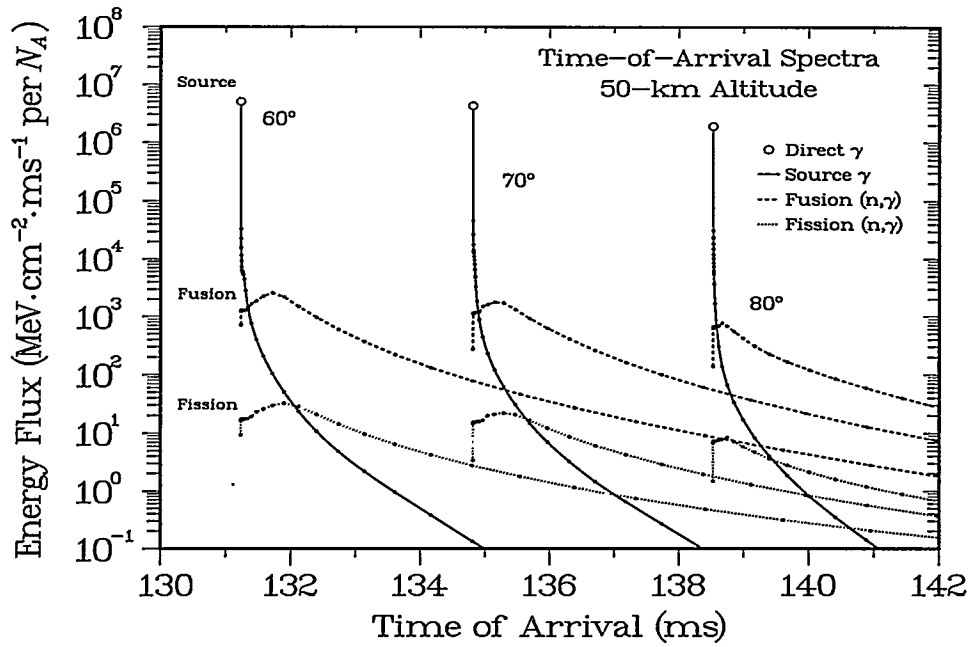


Fig. 5.1a. Time-dependent energy fluxes of source and secondary (n,n') gamma rays for 60°, 70°, and 80° angles with fusion and fission sources at 50 km.

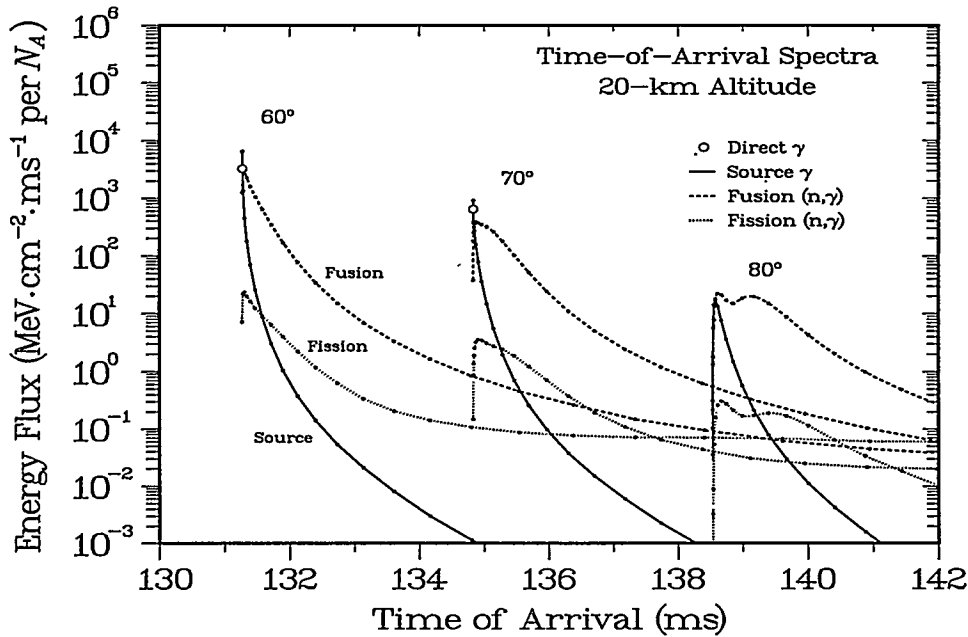


Fig. 5.1b. Energy fluxes as in Fig. 5.1a, but for sources at a 20-km altitude.

of the flux at the earliest times together result in a progressive delay in the arrival times for lower altitudes.

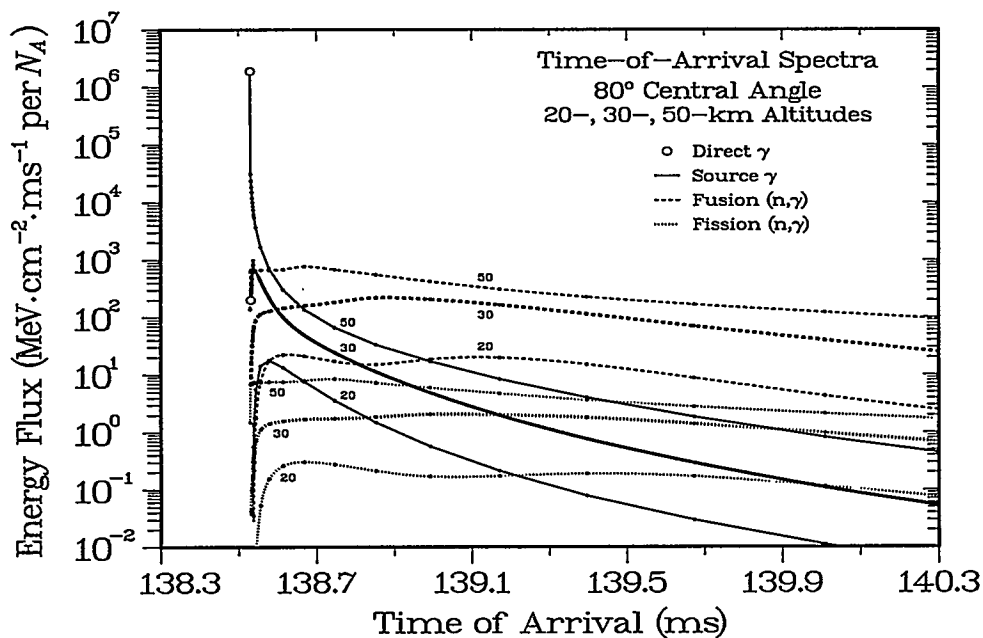


Fig. 5.2a. Time-of-arrival spectra for source and  $(n,n'\gamma)$  gamma rays from fusion and fission sources at  $80^\circ$  angles and at altitudes of 20, 30, and 50 km, as indicated by the small labels on each curve.

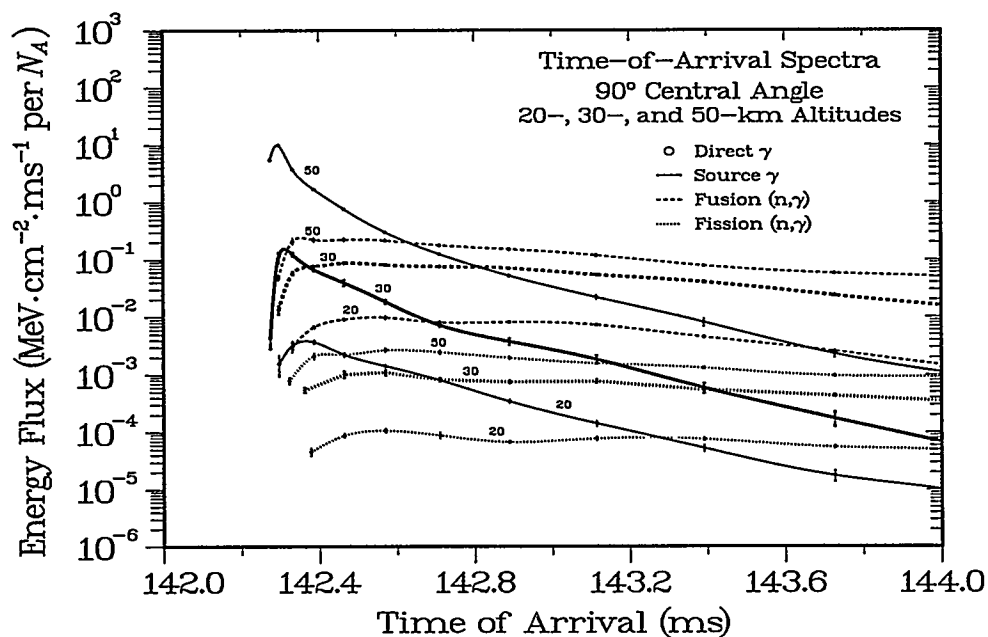


Fig. 5.2b. As in Fig. 5.2a, time-of-arrival spectra for fusion and fission sources, but for a  $90^\circ$  central angle.

**Summary.** At higher altitudes and more vertical angles, the large neutron interaction distances spread the  $(n,n'\gamma)$  production over relatively long times, which results in gamma-ray fluxes that are much lower than those from the nearly direct part of the source flux.



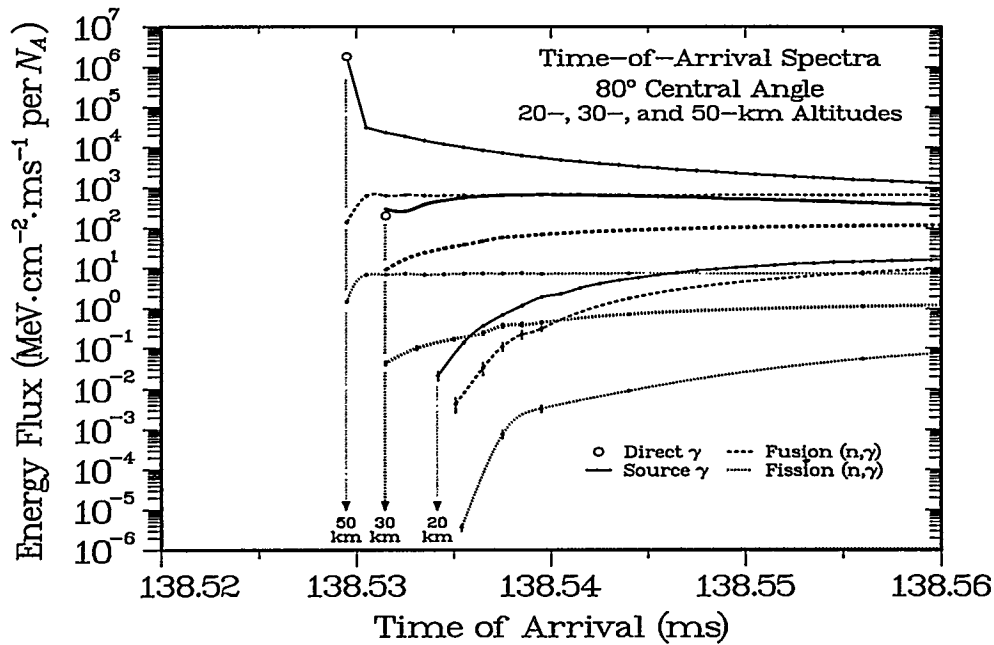


Fig. 5.3. High-resolution time-of-arrival spectra for sources at 80° angles and 20-, 30-, and 50-km altitudes, as indicated by the vertical arrows.

For fission sources, the secondary magnitudes are never competitive, but for fusion sources beyond the horizon the secondary fluxes can equal or exceed the source values. Because the relative advantage for secondary production increases with atmospheric density, we speculate that this effect may be significant for sources at even lower altitudes. As pointed out in Ref. 1, the large amounts of secondary gamma-ray production are somewhat expected, because  $(n,n'\gamma)$  reactions are a major mechanism for neutron inelastic scattering, especially at fusion energies. Note, however, that our results are normalized per mole of source particles, either neutrons or gamma rays, and additional information will be needed to obtain the actual output intensities for a particular source. Given that the observed signal is a combination of source and secondary components, the changing time behavior may provide both an identifying signature and a consistency check on the estimated source location.

## 6. SUMMARY AND CONCLUSIONS

**Calculation Layout.** The present report extends the atmospheric transport calculations of Ref. 1 well into the horizon region. This extension required significant changes in the calculational approach, especially the introduction of the powerful variance-reduction techniques provided by the MCNP code. In addition, the layout of the source and detector geometries was transformed from a single-source, multiple-detector arrangement to one with a single geosynchronous detector observing sources at different locations. Even with these improvements, about eight months of computer time and a total of  $5 \times 10^9$  gamma rays and neutrons were required for the calculations. Based on a suggestion in the previous study, finer graduations were introduced in the MCNP geometry for the upper atmosphere, which provides a better representation of scattering for over-the-horizon angles. This change in geometry is balanced against competing changes needed to provide

stability in the variance reduction. As a check, we also developed an analytical model for the unscattered portion of the gamma-ray energy transport, based on an angle- and altitude-dependent integral for the column density and the attenuation coefficients developed by Storm and Israel.<sup>5</sup> Finally, both the analytical and present Monte Carlo results were compared with those from the previous report and found to be in good agreement for angles extending almost to the horizon cutoff. Because the results are very sensitive to the assumptions about densities at the highest altitudes, however, their reliability will need to be carefully evaluated for any particular event of interest.

**Gamma-Ray and Neutron Transport.** For the calculations of standard transmissions and spectra, we have generally presented the results with relatively little discussion. An important exception is the comparison between the Monte Carlo and analytical approaches. Although the direct transmissions for both neutrons and gamma rays were well described, the complexity of the near-horizon case limits the usefulness of a strictly analytical approach for estimating the scattered component. In this situation, the similarity of the scattered transmissions for the gamma-ray, fission, and fusion source distributions may be an important starting point for the development of useful empirical approaches. For the moment, a candidate event can only be evaluated by the time-consuming process of interpolating between Monte Carlo results such as those in the present study. For gamma-ray measurements, this approach is further complicated by the coupling to the neutron flux introduced by the secondary (n,n') gamma-ray fluxes.

**Future Work.** The combination of the present and previous transport studies provides a strong foundation for the transition from generic sources to the more complex time and energy distributions of actual weapons, including the relative numbers of neutrons and gamma rays for different cases. Such calculations can begin by combining the basic outputs with calibrated detector responses<sup>7,8</sup> to provide realistic free-space count rates. In a subsequent step, the same problems can be studied with the additional complication of atmospheric transport, which can include the relative fluxes of primary and secondary gamma rays for specific cases. An initial version of such a study was presented in Ref. 9. Finally, the results of these more realistic simulations can be used as input to an effort to develop phenomenological techniques for automated signature analysis. Eventually, however, the calculational uncertainties will need to be carefully evaluated for each event of interest because of the sensitivity to details of the atmospheric model at high altitudes, including such issues as temporal variations in both composition and density.

## ACKNOWLEDGMENTS

The subject of this study was originally suggested by Jerry Conner and Rick Elphic of LANL, and their comments throughout the analysis were important to its development. The initial results and final manuscript were also discussed with Mike Meier, Paul Higbie, Ray Klebesadel, and Bruce Barraclough. The source file for the MCNP program was provided by John Hendricks of LANL's Transport Methods Group.

This work was supported by the Office of Research and Development of the U.S. Department of Energy's Office of Nonproliferation and National Security.

## REFERENCES

1. R. C. Byrd, "Atmospheric Transport of Neutrons and Gamma Rays from a High-Altitude Nuclear Detonation," Los Alamos National Laboratory report LA-12962-MS (July 1995) (U).
2. "U.S. Standard Atmosphere, 1976," U.S. Government Printing Office, Washington, DC 20402 (October 1976) (U).
3. J. F. Briesmeister, Ed., "MCNP-A General Monte Carlo N-Particle Transport Code, Version 4A," Los Alamos National Laboratory report LA-12625-M (November 1993) (U).
4. George Auchampaugh, "Atmospheric Neutron Leakage Spectrum from a Hypothetical Endoatmospheric Nuclear Detonation as Viewed from Space (U)," Los Alamos National Laboratory report LA-12424-MS (CRD) (September 3, 1992).
5. Ellery Storm and Harvey I. Israel, "Photon Cross Sections from 0.001 to 100 MeV for Elements 1 through 100," Los Alamos Scientific Laboratory report LA-3753 (November 1967) (U).
6. R. C. Byrd, G. P. Estes, and C. R. Mannon, "Far-Field Fast-Neutron Energy Spectra from an Unshielded Fission Reactor," Los Alamos National Laboratory report LA-12870-MS (March 1995) (U).
7. R. C. Byrd, J. D. Drabanski, and B. L. Barraclough, "Monte Carlo Calculations of the Effective Area and Directional Response of a Polyethylene-Moderated Neutron Counter," Los Alamos National Laboratory report LA-12850-MS (January 1995) (U).
8. R. C. Byrd, "Calculations and Measurements of the Energy-Dependent Response of a Shielded Gamma-Ray Detector," Los Alamos National Laboratory report LA-13030-MS (in production) (U).
9. R. C. Byrd, "Atmospheric Transport of Neutrons and Gamma Rays from High-Altitude Nuclear Detonations (U)," Los Alamos National Laboratory report LA-13051-MS (SRD) (November 29, 1995).

